I. FIELD ION MICROSCOPE STUDY OF DILUTE
PLATINUM COBALT

II. TRANSPORT MEASUREMENTS ON HIGH PURIT
TUNGSTEN AT ULTRA-LOW TEMPERATURES

Dissertation for the Degree of Ph. D.

MICHIGAN STATE UNIVERSITY

EARL LEWIS STONE III

1976

ABSTRACT

- I. FIELD ION MICROSCOPE STUDY OF DILUTE PLATINUM COBALT
- II. TRANSPORT MEASUREMENTS ON HIGH PURITY
 TUNGSTEN AT ULTRA-LOW TEMPERATURES

By

Earl Lewis Stone III

- I. Alloys of 0.6, 1.7 and 3.7 at% cobalt in platinum were examined in a field ion microscope using pulsed field evaporation. Images of pure platinum control specimens and of alloy specimens were compared to establish the types of signatures produced by the cobalt atoms. The cobalt atom signature was found to be a single dark atomic site. For the 3.7 at% alloy, the exact sites of a large number of cobalt atoms in the lattice were determined from measurements of the cobalt signature positions. Normalized radial distribution functions were calculated and found to be consistent with a random distribution for cobalt atoms in platinum.
- II. Measurements are reported of size dependent electrical resistivity, and of electrical resistivity and

thermoelectric ratio, G, at ultra-low temperatures for high purity, single crystal tungsten. A generalized version of the Nordheim model is used to derive a lower bound upon the size dependent resistivity, assuming that surface scattering is completely diffuse. Measurements are presented which fall below this lower bound indicating, within the framework of the model, the presence of specular scattering. Electrical resistivity measurements on two high purity samples were consistent with the equation $\rho = \rho_o + AT^2$ from 1.8 K down to below 0.1 K. This quadratic variation of resistivity down to such low temperatures is attributed to electron-electron scattering. For the highest purity sample, the thermoelectric ratio G behaved simply and in accord with expectations. For two less pure samples, G behaved anomalously at ultra-low temperatures.

- I. FIELD ION MICROSCOPE STUDY OF DILUTE
 PLATINUM COBALT
- II. TRANSPORT MEASUREMENTS ON HIGH PURITY
 TUNGSTEN AT ULTRA-LOW TEMPERATURES

Ву

Earl Lewis Stone III

A DISSERTATION

Submitted to
Michigan State University
in partial fulfillment of the requirements
for the degree of

DOCTOR OF PHILOSOPHY

Department of Physics

ACKNOWLEDGMENTS

My sincere thanks go to my advisor, Dr. Jack Bass, for his advice, assistance and encouragement throughout the thesis project. I wish to thank Dr. Moshen

Khoshnevisan for the development of our field ion microscope system. I am indebted to Dr. J. M. Galligan for a tungsten specimen and to Mr. B. Addis for preparing the platinum cobalt alloy wires and for providing a tungsten specimen. I would like to acknowledge and express my appreciation to the Cornell group of Professors Seidman and Balluffi, and their graduate students for many useful suggestions on field ion microscope techniques. Finally, I wish to thank my wife, Diana, for her encouragement and assistance in preparing this thesis.

TABLE OF CONTENTS

														Page
LIST OF	TABLE	s.	•	•	•	•	•	•	•	•	•	•	•	vi
LIST OF	FIGUR	ES .	•	•	•	•	•	•	•	•	•	•	•	vii
	PAR	T I. OF	FI DIL								UDY			
Chapter														
ı.	INTRO	DUCT	ION	•	•	•	•	•	•	•	•	•	•	2
	D. E. F.		ifac tial Sys	llog Allo t S: Dis tem	y Stoy S ite: str:	tud. Stu s	ies die	s						
II.	EXPER	IMEN'	TAL	PRO	CEDU	JRE	•	•	•	•	•	•	•	9
	А. В. С.	1. 2. 3. FIM	Wir FIM	tial e Ti Tip Dat	l Sa read o Ma ta A	ampi tmen akin	le : nt ng	Pre	-					
III.	THE C	OBAL!	r si	GNA	ruri	2	•	•	•	•	•	•	•	22
	A. B. C.	Conf Allo 1. 2.	mica trol by S The The Atom	Speci peci 0.6 1.7	ecir imer 5 at 7 ar 7s	nens 18 18 (1 1d)	s Co : 3.7	at!	e C	o i	n Pi		nce	

Chapter		Page
IV.	SPATIAL ANALYSIS	40
	A. Lattice Coordinates and Transforma- tion	
	 Relative Coordinates on One Layer Shift for Successive Layers Nonideal Image 	
	B. Radial Distribution Function 1. Definitions	
	2. Types of Spatial Distributions	
	 Correction for Coordination Numbers 	
	C. Data and Results	
	 The 3.7 at% PtCo Alloy Correction for Artifacts 	
	D. Discussion	
	PART II. TRANSPORT MEASUREMENTS ON HIGH PURITY TUNGSTEN AT LOW AND ULTRA-LOW TEMPERATURES	
٧.	SIZE DEPENDENT ELECTRICAL RESISTIVITY IN TUNGSTEN	59
	A. Introduction	
	B. Theory	
	C. Samples D. Experimental Data and Analysis	
	D. Daperimental Data and Intaly 515	
VI.	ELECTRICAL RESISTIVITY MEASUREMENTS IN TUNGSTEN AT ULTRA-LOW TEMPERATURES	69
	A. Introduction	
	B. Experimental Procedure	
	C. Results and Discussion	
VII.	THERMOELECTRIC RATIO MEASUREMENTS IN TUNGSTEN AT ULTRA-LOW TEMPERATURES	79
	A. Introduction	
	B. Present Study	
LIST OF	REFERENCES	90

		Page
APPENDIX	A: DETAILS OF COMPUTER ANALYSIS	97
	Digitizing and Sorting 1. Layer Origin Data Record 2. Co Site Data Record 3. All Atom Data Record	
	Transforming Scanner Coordinates to Planar Coordinates	
C.	Transforming Planar Coordinates to FCC Cartesian Coordinates	
D.	Shift of Origins for Successive Layers	
	Radial Distribution Function Calculation	
	The Significance of the Transformation Parameters	
G.	Flow Chart of Computer Programs	
APPENDIX	B: BASIC PRINCIPLES OF THE FIELD ION MICROSCOPE	110
B. C. D.	The Basic Apparatus Field Ionization Resolution of the FIM Focusing Field Evaporation	

LIST OF TABLES

Table			Page
3A.	Chemical Analyses	•	23
3B.	Test of Homogeneity	•	24
3C.	Test of Strain-anneal Procedure	•	25
3D.	Semi-quantitative Spectrographic Analysis .	•	26
3E.	Control Run Set I on Pure Platinum	•	28
3F.	Control Run Set 2 on Pure Platinum	•	29
3G.	Results for 0.6 at% PtCo Alloy Tips	•	34
3н.	Results for 1.7 at% PtCo Alloy Tips	•	36
31.	Final Results for 1.7 at% PtCo Alloy Tips .	•	36
3J.	Results for 3.7 at% PtCo Alloy Tips	•	37
3K.	Final Results for 3.7 at% PtCo Alloy Tips .	•	37
4A.	Average Effective Coordination Numbers	•	52
4B.	Number of i th Nearest Neighbor Pairs in 3.7 at% PtCo	•	53
4C.	Artifact Nearest Neighbor Pairs in Pure Pt	•	54
6A.	Values for the Coefficient A	•	78
7A.	Reported Impurity Concentrations	•	88
AA.	The Transformation Parameters	•	103

LIST OF FIGURES

Figure			Page
2A.	Calibration curve for PtCo alloys		. 12
2B.	Schematic layer of atoms		. 21
3A.	Field ion micrograph of Pure Platinum Ti	.p	. 27
3B.	Field Dissection of a {315} plane		. 32
3C.	Field ion micrograph of a 3.7 at% PtCo t	ip	. 33
4A.	Ball model of {315} plane		. 42
4B.	Schematic of {315} plane		. 42
4C.	Ball model of {213} plane		. 43
4D.	Schematic of {213} plane		. 43
4E.	Pattern for clustering		. 49
4F.	Pattern for short range order		. 49
4G.	Normalized radial distribution function		. 56
5A.	Inverse RRR's of tungsten wires		. 66
6A.	Resistances of tungsten samples versus T below 2°K	.2	. 75
6B.	Resistances versus T, T^2 , T^3 below $1^{\circ}K$.		. 76
7A.	Thermoelectric ratio of tungsten	,	. 82
7B.	Thermoelectric ratio below 1°K	,	. 84
7C.	Pseudo-thermopower below 0.3°K		. 86
AA.	Sorting program	•	. 107
AB.	Body of main program		. 108
AC.	Plotter program		. 109

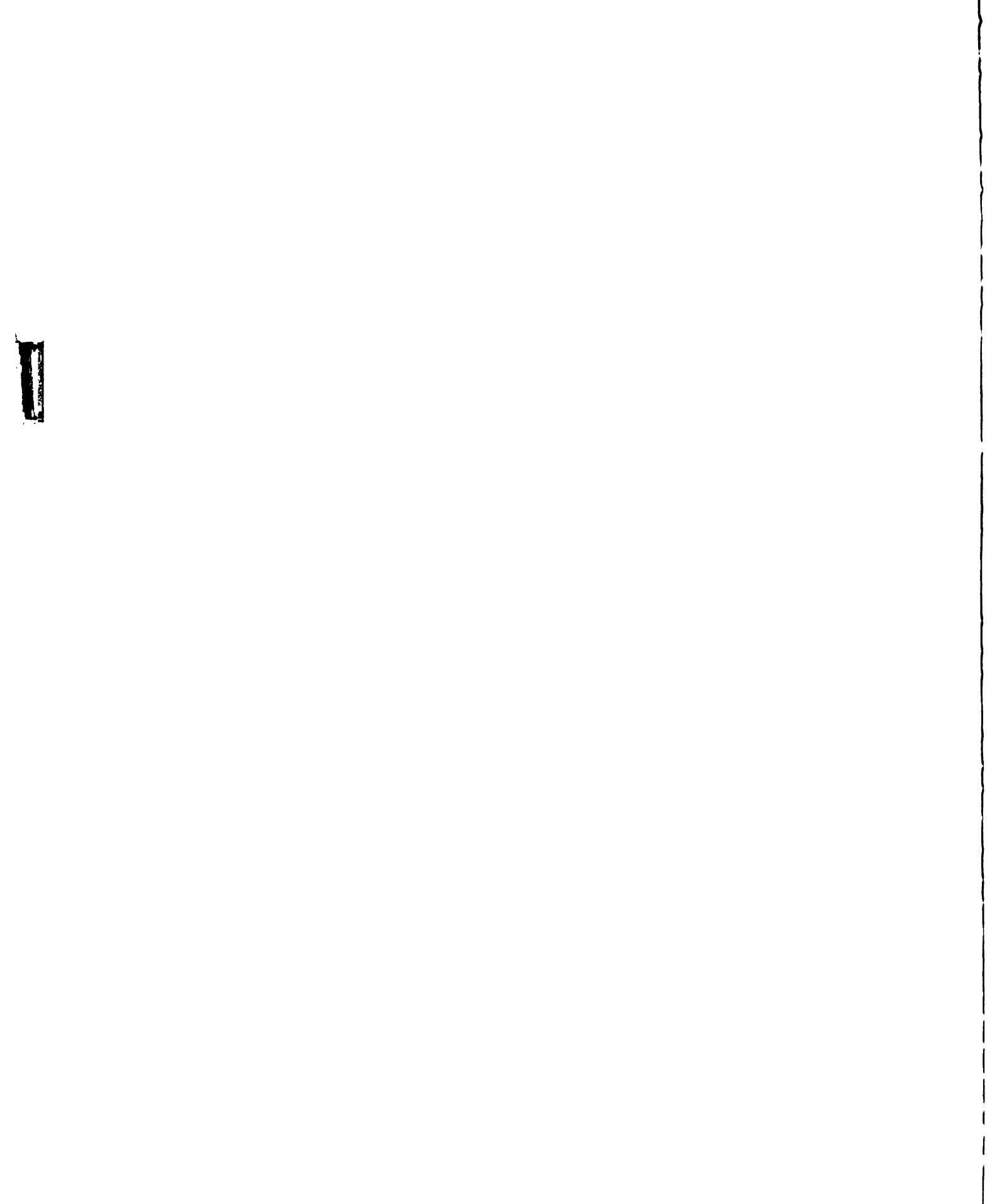


Figure		Page
BA.	Schematic diagram of a glass field ion microscope	112
BB.	One-dimensional potential energy diagrams for field ionization	114
BC.	(After Müller); Motion of the imaging gas atoms near the tip surface	120

PART I

FIELD ION MICROSCOPE STUDY OF DILUTE PLATINUM COBALT

CHAPTER I

INTRODUCTION

The field ion microscope (FIM) is a tool which has atomic resolution, allowing visualization of atoms as well as individual defects and impurities in a crystal lattice. With the FIM, direct determination of the microscopic spatial distribution of solutes in alloys can be made. Analysis of all other types of experimental data only allows inferences concerning this distribution.

The present FIM study is an investigation of alloys which have dilute amounts of cobalt (Co) in platinum (Pt). For this reason, the specific examples and special procedures discussed will be of the PtCo alloys. For those with no knowledge of the FIM, the basic components and principles of operation are described in Appendix B, which is a verbatum reproduction of Appendix A from the thesis of M. Khoshnevisan (1).

A. Development of the FIM

The FIM was introduced by Müller (2) in 1951 and has been developed over the years to where it is now a useful quantitative tool. The first major advance in field ion microscopy was the realization in 1955 that by

cooling the FIM, atomic resolution of large sections of the specimen could be obtained (3). At the same time, the discovery of field evaporation (4) made possible the imaging of FIM tips with a high degree of surface perfection. It also made possible the slow dissection of a bulk specimen. The development of the ability to resolve large sections of a specimen atomically layer by layer opened up the possibility of determining the spatial distribution of defects and impurities in metals and alloys.

B. Early Alloy Studies

Many early alloy studies were concerned with establishing the signature of solute atoms, that is, determining how a solute atom would appear in the FIM image. Positive identification of solute atoms in the host material was necessary before any study could be made of their spatial distribution. Early investigations of binary alloys showed only that in general the image became more irregular as the solute content increased (5, 6). Image interpretations of alloys could be made using ordered binary alloys because of their high degree of surface pattern perfection. The signature of Co in PtCo alloys was the first to be identified. Southworth and Ralph (7) and Tsong and Müller (8, 9, 10) inferred from their studies of ordered PtCo alloys that Co atoms in Pt were invisible. That is, while Pt atoms appeared

as bright spots in regular arrays, Co sites were not imaged, therefore appearing as dark spots (i.e., as vacant sites).

C. Dilute Alloy Studies

Image interpretation was also possible in dilute Small concentrations of impurities do not seriously degrade the surface pattern perfection of the host material. Dubroff and Machlin (11, 12) made FIM studies of platinum and tungsten based alloys. inferred that for cobalt, nickel, gold, and palladium in platinum, the solute signature was a vacant site. were, however, serious discrepancies between the observed vacant site concentrations and the nominal solute concentrations. Two complementary explanations have been proposed for the discrepancies (13). First, it is now known that the {102} plane, on which they did their study, has an artifact vacancy concentration of one to two atomic percent, even in a well-annealed pure Pt tip (14, 15). Thus, the {102} plane was inappropriate for any quantitative studies. Second, the actual solute content was not determined by independent means. The one specimen that was analyzed turned out to have only 5.7 at% instead of the nominal 10 at% gold in platinum. For these reasons, their study gave only qualitative support for their suggestion. It was not until a study by Chen (13, 16) that a quantitative correspondence between nickel and

gold atoms in platinum and vacant sites was made. Chen made the proper background studies of pure platinum and also independently verified the solute concentration of the alloys by chemical analysis.

D. Artifact Sites

In any FIM study, one major problem is artifact sites, that is, spurious vacant sites in the middle of a These can be mistaken for vacancies in quenching studies or for solute sites in alloy studies. In well annealed pure Pt, the concentration of artifacts observed are orders of magnitude greater than that expected from the equilibrium vacancy concentration. Therefore, it is evident that artifacts must be sites where a host atom was pulled off the surface. This means that before any serious quantitative studies can be done, it is first necessary to study pure Pt in order to determine which planes have sufficiently low background levels of artifacts. These control runs are critical and must be made under the same experimental conditions as the alloy Once the planes in the pure Pt with background levels of at least an order of magnitude less than the planned solute concentrations have been found, alloy studies can proceed. Independent determinations of alloy concentrations by chemical analysis are then made. Only if the concentrations of signatures from the FIM analysis

agrees with these independent assays can the correspondence of signature to solute atom be made with confidence.

E. Spatial Distribution

Once the type of solute signature in the host has been positively identified and a one to one correspondence between this signature and the solute atom has been verified, detailed microscopic analysis can begin. The procedure is to record the positions of the solute atom lattice sites in terms of a surface coordinate system and then to transform these positions into a bulk system representative of the crystal structure of the alloy. For dilute concentrations of Co in Pt, this is face-centered-cubic (FCC). From this point it is relatively straight-forward to calculate the actual spatial distribution, or some other parameter of interest. These directly determined parameters can then be used to examine inferences drawn from other less direct experiments.

F. FIM System

The all metal and glass FIM system used in the present study has been specially designed for quantitative work. The provisions for ultrahigh vacuum, internal image intensification, liquid and gaseous helium cooling, and automatic pulsing and photographic recording make this possible. The details of the FIM system have been described in a thesis by Khoshnevisan (1).

One serious problem in FIM studies is the high failure rate of tips. It is the source of greatest experimental difficulty. This has been partially overcome in this system by the use of a unique five-sample rotator designed by Khoshnevisan and Stephan (17).

G. Present Study

With this specially designed system, the actual spatial distributions of alloys can be determined and the inferences from other experimental work examined. Schwertfeger and Muan (18) have made thermodynamic measurements of disordered PtCo alloys in the temperature range of 1200-1400°C. Their results indicate that the PtCo system displays a strong tendency for ordering at these temperatures. There are also diffuse x-ray scattering measurements of PtCo, at 860°C, by Rudman and Averbach (19). Their short range order parameters for PtCo are negative, also suggesting an ordering tendency. These experiments were done on more concentrated alloys at elevated temperatures. How well these results carry over to more dilute alloys at temperatures below 860°C is unknown. Several susceptibility and resistivity studies on dilute PtCo alloys have been made in recent years (20, 21, 22). The data are usually fit to theories which assume a random distribution of Co in Pt. With the system mentioned above, it should be possible not only to quantitatively confirm that the signature of a Co atom in Pt is a vacant site, but also to determine the radial distribution function which would specify whether dilute Co in Pt alloys at lower temperatures exhibit clustering, randomness, or short range order. This should provide an accurate spatial distribution as a sound basis for theoretical work.

CHAPTER II

EXPERIMENTAL PROCEDURE

A. Specimen Preparation

1. Initial Sample Preparation

The platinum and platinum alloy samples were made by Bud Addis, Material Science Center, Cornell University. He prepared alloys of 0.6, 1.7, and 3.7 atomic percent cobalt in platinum using an arc melter. The alloys were arc melted several times to insure homogeneity before being drawn into 8-10 mil diameter wires. For control and background purposes, pure platinum was also given the same treatment, being arc melted several times, then drawn into a 10 mil diameter wire. Upon receipt of these wires, several portions were removed for atomic absorption and neutron activation analysis.

2. Wire Treatment

When received, the wires were first rinsed and wiped with methanol to remove surface dirt, then cleaned in aqua regia, and finally rinsed in distilled water and methanol to remove any remaining surface contamination. Single crystal endforms on the specimen wires are needed to provide the necessary clear image for counting atoms

and vacant sites in the FIM. To insure the growth of large enough single crystal grains for proper endforms, the following strain-anneal procedure was used. The wires were heated briefly, approximately 30 seconds, to a slight red glow in vacuum to reduce cold work. They could then be drawn down through diamond dies into 5.5 mil wires without breaking. They were cleaned in aqua regia and methanol between draws to remove surface contamination. The 5.5 mil wires, in lengths of about 30 cm, were heated to approximately 1000°C for one hour in vacuum. They were then drawn to 5.0 mils. The final anneal was for twelve hours at about 1000°C in vacuum. The vacuum in all cases was better than 5 x 10⁻⁶ torr.

The wires were heated resistively with their temperatures determined by the resistance ratio R(T)/R(20°C). For pure platinum, a calibration table exists, but not for the alloys (23). To make calibration tables for the alloys, simultaneous measurements of R(T)/R(20°C), using standard four probe techniques, and of temperature, using a calibrated optical pyrometer, were made. Samples of the alloys were heated resistively in air where they could be observed directly, thereby avoiding problems of calibration through glass. The pyrometer was checked by making identical measurements on a pure platinum wire. Before measuring the base resistance R(20°C), the alloy wires were heated briefly to a red glow to remove the

major effects of cold work. In Figure 2A the calibration curves for the alloys are presented.

No phase separation occurs for dilute amounts of cobalt in platinum (24). This simplified the characterizing procedure, allowing the anneals to be ended by slowly turning down the current through the wires over a period of about a minute. The pure platinum wires used for background counting and controls were given the same treatment as the alloy wires.

Calculations of an effective freeze-in temperature (T_f) were made based on the diffusion data of Co in Pt by Kucera and Zemcik (25). Since the endforms were single crystal, it was assumed that only volume diffusion was present. Samples with large numbers of dislocations would not have been imaged due to tip failure at the high voltages used. The diffusion coefficient, D, is usually expressed as:

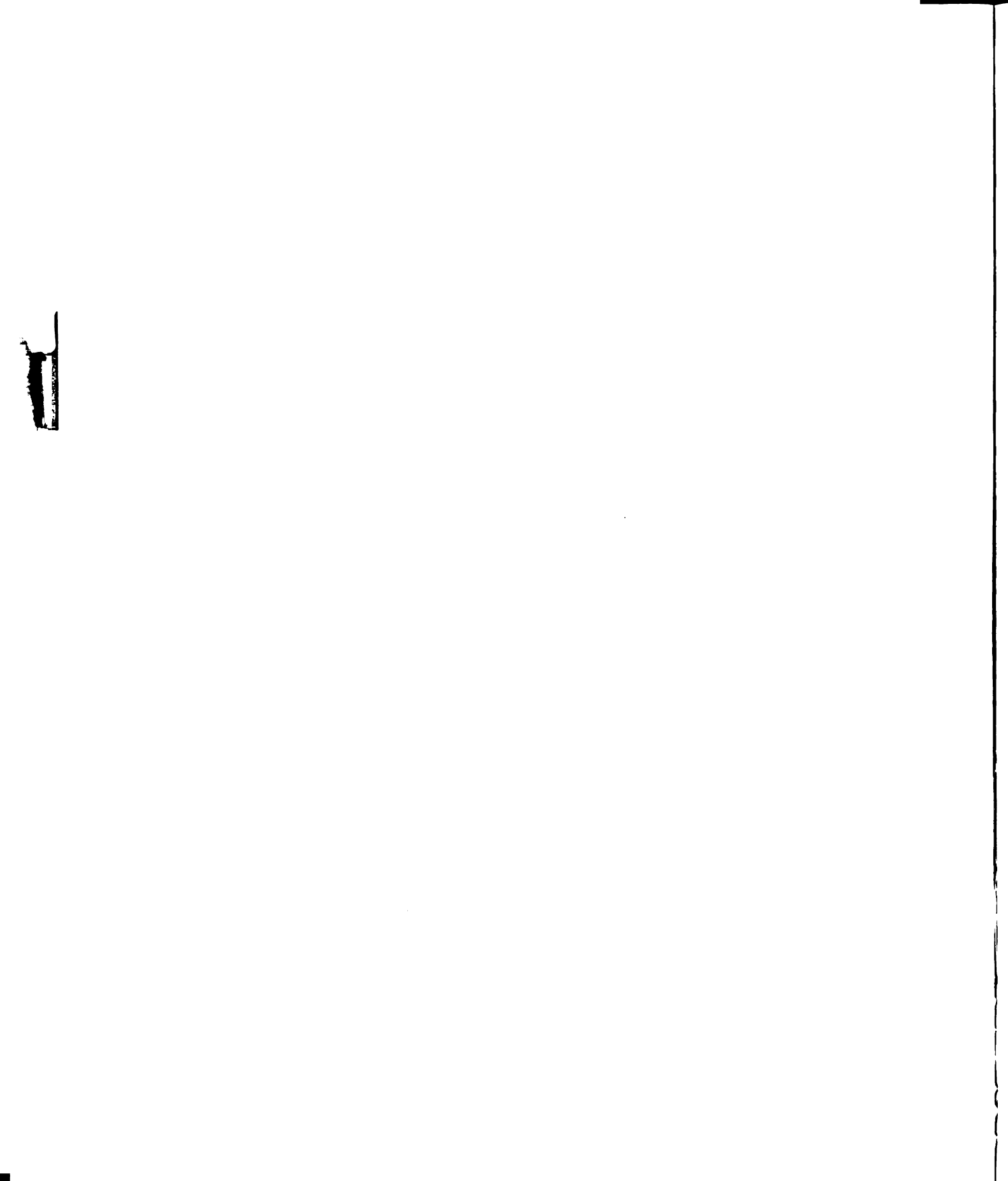
$$D = D_{O} \exp(-\frac{Q}{RT})$$

where D_{O} is a frequency factor,

Q is the activation energy in Kcal/mole

R is the gas constant of 1.987 x 10^{-3} Kcal/mole deg., and T is the absolute temperature in degrees Kelvin.

The values obtained by Kucera and Zemcik in the temperature range 1170 to 1320°K for $D_{_{\rm O}}$ and Q are 19.6 cm²/sec



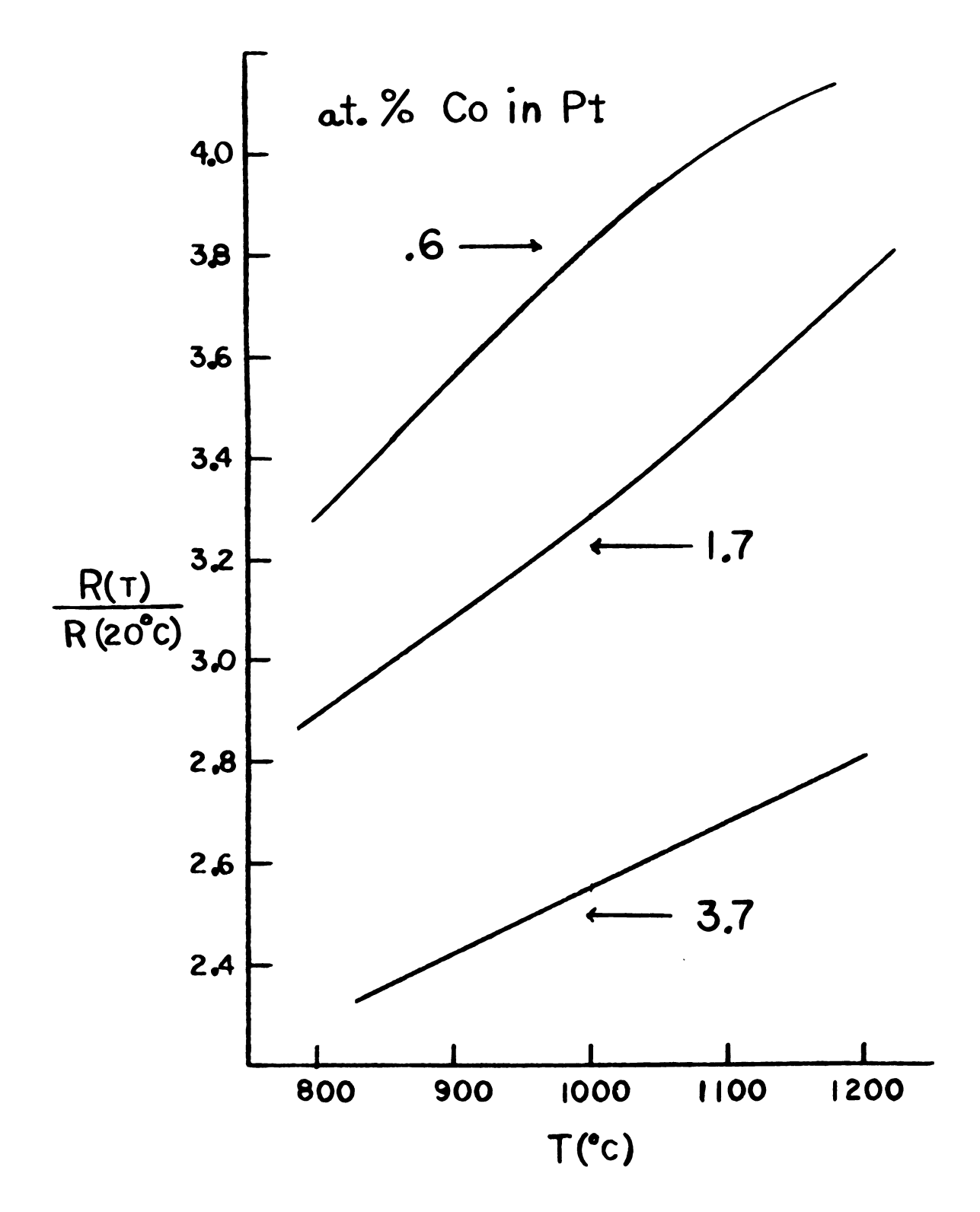


Figure 2A.--Calibration curve for PtCo alloys.

and 74.2 Kcal/mole respectively. They then decomposed these data into the sum of two terms: volume diffusion, with values of $D_{\rm O} = 156~{\rm cm}^2/{\rm sec}$ and $Q = 80.1~{\rm Kcal/mole}$, and diffusion along high diffusivity paths.

In view of the uncertainty in this decomposition, determination of a freeze-in temperature must be only approximate. The freeze-in temperature for the purposes of this calculation is defined to be that temperature where the average motion \overline{X} of a Co atom is on the order of the lattice spacing a_0 during a time interval Δt . This time interval is determined by the cooling rate through the freeze-in temperature. The cooling rate of the wire specimens was about 17 deg/sec. In the temperature range of interest, the diffusion coefficient changes by about a factor of ten in a three second interval. A choice, then, of $\Delta t = 1$ sec specifies a temperature range such that if the Co atoms are slowly moving at the top end, they are effectively at rest at the lower end. An estimate of the average motion \overline{X} is

 $x = \sqrt{4D\Delta t}$

The choice of \overline{X} equal to a lattice spacing ($a_0 = 3.92$ Å for Pt) leads to a value of D at the freeze-in temperature of 4×10^{-16} cm²/sec. Putting this value of D into the expression for the diffusion coefficient and solving for the freeze-in temperature yields $T_f \approx 1000$ °K. Due to

the approximate nature of the calculation and the uncertainties in $D_{\rm O}$ and Q, this freeze-in temperature estimate is good to \pm 50°K (if one chose $D_{\rm O}$ = 19.6 and Q = 74.2, the calculated freeze-in temperature would be 50° higher). The 1000°K freeze-in temperature is 400-600°K less than the temperatures used in the activity measurements (18), but only slightly lower than those used in the x-ray determination of the local order parameter (19).

A check on the effect of the anneal and the drawing on composition was made. Several portions of the alloy wires that had been through the annealing procedure and others that were drawn straight into 5.0 mil wires were set aside for neutron activation analysis. These analyses were compared with those done on the wires as received.

3. FIM Tip Making

From one 30-cm piece of annealed wire about 20 one-cm pieces were cut with scissors. Portions near each end of the large wire, where the annealing temperature had been lower, were not used. One end of each small piece was spot welded onto a 10 mil diameter platinum wire hook. The other end was then electropolished down to a diameter of about 300 Å for the FIM tip.

A standard electropolishing method using a molten salt solution of $NaNO_3$ and 13% NaCl by weight at about

360°C was used to taper the tips to a sharp point (26, 13). A voltage of 1-2 volts DC was used with the tip as anode. The salt mixture was melted in a pyrex beaker that had been wound with resistance wire, covered with a layer of furnace cement, and set in a fire brick. The temperature of the molten salt was controlled by varying the current through the resistance wire with a variac. The temperature was monitored with a Chromel-Alumel thermocouple.

Each tip was first immersed for approximately five minutes to remove any dislocation damage from the cutting and to produce a generally tapered shank. The tips were then alternately dipped for a few tenths of a second and observed under a 440 X light microscope until the required sharp tip was obtained. A combination of the taper angle and the pattern of the Fresnel fringes around the end of the tip was examined to determine when the tip was sharp enough (1). The tips were inspected twice, the second time with the shank rotated 90° to check for chisel-shaped tips, which would give an undesirably elongated image in the FIM. The tips and their 10 mil platinum wire hooks were then spot-welded onto 40 mil tungsten rods and mounted in the FIM.

An advantage of the molten salt solution was that it polished more uniformly on the sides than an acid mixture (${\rm H_3PO_4}$, ${\rm H_2SO_4}$, ${\rm HNO_3}$) or aqua regia. The possible

redistribution of the solute during the tip immersion in the 360°C molten salt was not a problem. Even with the five-minute (300 sec) immersion times and possible enhancement of diffusion by vacancies, the average atomic motion is only 0.1 a_o as calculated using the following information. At 360°C, the volume diffusion coefficient D is 3.4 x 10^{-26} cm²/sec. An upper bound on the vacancy enhancement of the diffusion is the ratio of the number of vacancies at the annealing temperature to that at 360°C

$$\frac{C_{v}(1000^{\circ}C)}{C_{v}(360^{\circ}C)} = 3.6 \times 10^{5}$$

where $C_V^{}(T)$ is the concentration of vacancies at temperature T. $C_V^{}(T)$ is usually expressed as:

$$C_{v}(T) = C_{o} \exp \left(-\frac{E_{f}}{kT}\right)$$

where C is a constant.

 ${\tt E}_{\tt f}$ is the formation energy of a vacancy, in this case taken as 1.4 eV for Pt,

K is the Boltzmann constant, and

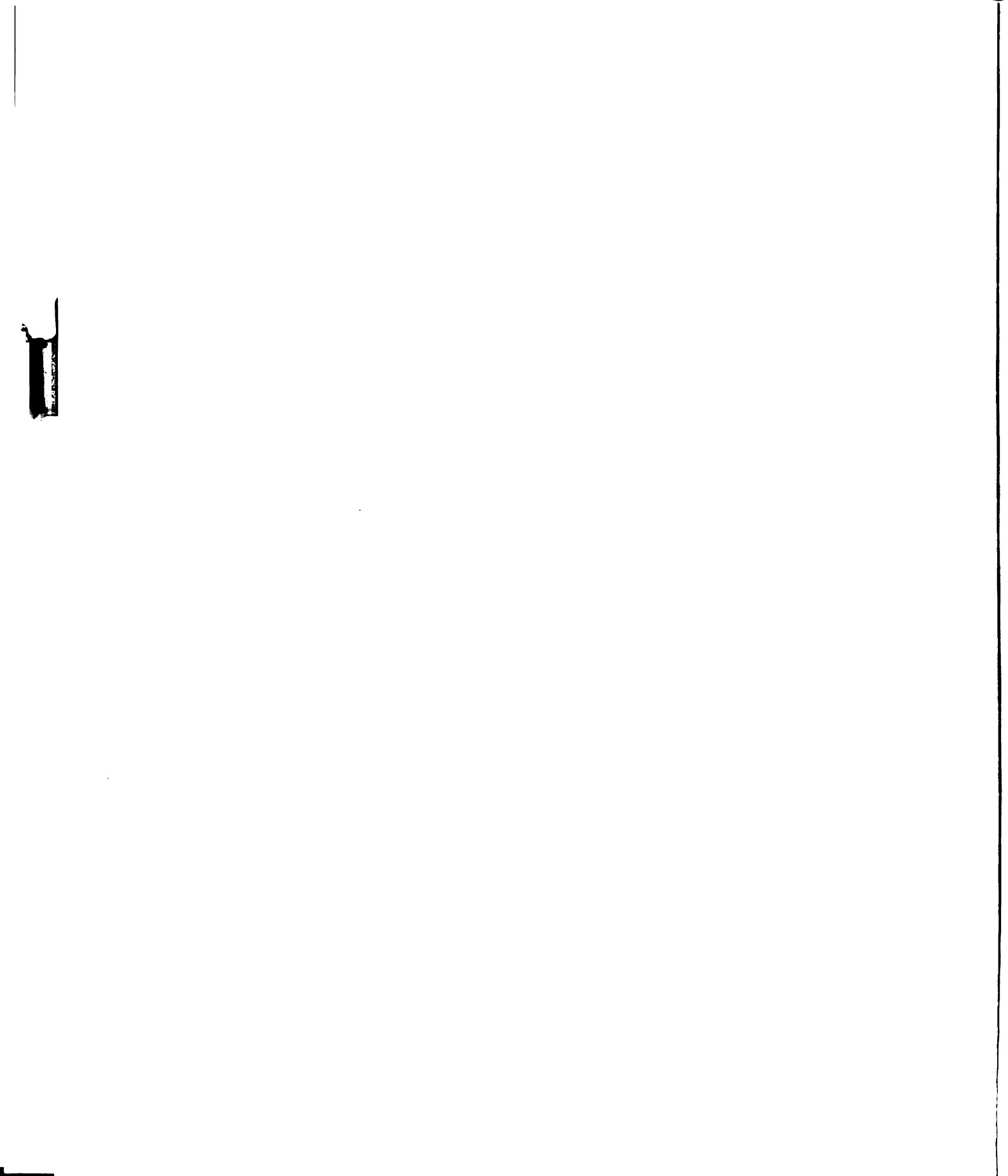
T is the absolute temperature in degrees Kelvin. In the dipping process, the total immersion time was usually about 30 seconds, the average total time to make one tip was 1/2 hour. About 1/3 to 1/2 of the wire

pieces immersed were finally made into tips sharp enough for use in the FIM.

B. FIM and Data Acquisition System

The FIM and photographic recording system used are very similar to those described by Khoshnevisan (1). One change was the addition of a titanium sublimation pump, which allowed the removal of residual or outgassed oxygen and nitrogen. This was especially important when the FIM was operated in the static mode for the earliest runs on pure Pt and on the 0.6 at% PtCo. For static mode operation, the FIM was closed off from the pumping system, and helium imaging gas was leaked through a heated pyrex tube to backfill the system to a gauge reading of 5 x 10⁻⁴ torr. In an effort to cut down the possibility of contamination, the system was later changed so that it could be operated in a dynamic mode. mode, spectroscopically pure helium was leaked through a Varian leak valve to run at a gauge pressure of 5×10^{-5} torr with the pumps still opened to the system.

The FIM run procedure was as follows. Five tips were loaded into the microscope body and the body inserted and bolted to the ultra-high vacuum (UHV) system. The system was roughed out using a Vacsorb pump and then pumped out further using a diffusion pump. A liquid nitrogen cold trap prevented diffusion of any oil into the vacuum chamber. The system was then baked at



175°C for four hours. With twelve hours of pumping, vacuums of 2×10^{-9} torr were routinely obtained. The specimens were cooled to about 80°K by filling an outer liquid nitrogen jacket. The system was then backfilled with pure helium imaging gas.

The DC voltage on the tip was raised slowly until the tip was evaporated to a nearly perfect hemispherical endform. The first image spots usually appeared around 2 KV, then a motor driven pot was used to slowly ramp up the voltage at 0.8 KV/hr. Only about one in five tips was evaporated to a good usable endform, normally about 7 KV, without failing. The advantage of the five sample rotator system was that, after a tip failure, the high voltage could be quickly lowered, a new FIM tip rotated into position and started in about 10 minutes, without breaking vacuum.

When a suitable endform was obtained, the system and the tips were further cooled by means of a continuous liquid-gas helium transfer system. Varying the rate of pumping on the system allowed temperature regulation between 20 and 60°K. Normal running temperature was 30°K.

The camera system was positioned and a test strip taken to check the focus and the exposure settings. To insure a clean surface, a final ten layers of a {102} plane were then peeled off before actual filming. The specimen was dissected atom by atom using pulsed field

evaporation technique and the image was synchronously recorded (15, 1). The voltage pulses and the camera were controlled by a 'pulser' control box. The 'pulser' first operated the camera to expose a frame, then triggered a square wave voltage pulse. The field evaporation pulse was amplified and applied to the FIM tip. In normal operation, voltage pulses of about 400 V and 3 milliseconds duration were used, with the height being adjusted so that the tip evaporated slowly at a rate of about 80 pulses per layer as counted on a {102} plane.

An internal Bendix channel plate and postacceleration of the electrons was used for image intensification. This allowed exposure times of about 1/2
second and repetition rates of about 1 second.

The FIM images were recorded on 400 foot lengths of 35 mm Kodak Double-X film using an Automax camera.

The film was then developed at the MSU Photo Lab.

C. Film Analysis

The preliminary film analysis was done using a Vanguard motion analyser. Each film was run through the motion analyser several times with one particular crystallographic plane being watched during each scan. When a signature was seen, the frame number corresponding to the location on the film was noted along with the type of signature. The number of layers peeled through and the average number of atoms per plane were also recorded.

The following criteria were employed for counting both atoms and sites. They were counted immediately after the last atom of the preceding layer was completely evaporated. A schematic layer of atoms and the outer ring of atoms (solid line) is shown in Figure 2B. This outer ring was disregarded to avoid the ambiguity that would arise if a vacant site, such as site A, occurred on it. It is difficult to decide if such a site is actually a Co site or simply due to irregular evaporation. Therefore, only those sites which could be positively identified, such as site B, were counted. From one layer to the next, the general shape of the outer ring for a particular plane remained roughly the same with some variation in the number of atoms on each layer.

The film analysis necessary for the spatial distribution was done using the High Energy Physics scanning tables. The scanning table is a setup by which the relative positions of the atom images can be digitized and recorded on magnetic tape. These tables have crosshairs that can be positioned to within 0.001 inch. The typical separation of atoms on the scanning tables was 0.075 to 1.25 inches. Even on less distinct dots, the crosshairs could be easily repositioned over an atom to within ± 0.005 inch. The data on the magnetic tape were then fed into the computer programs to be handled as described in the analysis chapter.

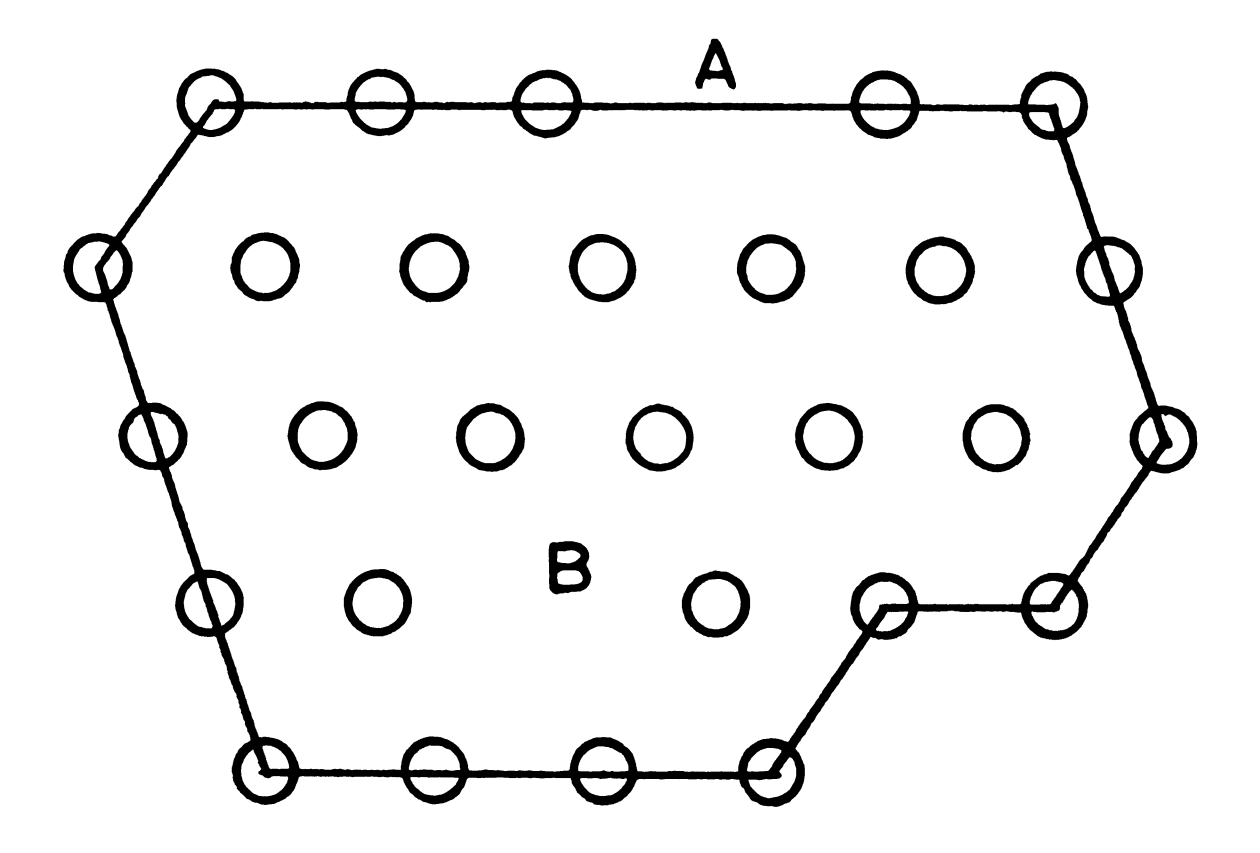


Figure 2B.--Schematic layer of atoms.

CHAPTER III

THE COBALT SIGNATURE

A. Chemical Analysis

Portions of each of the as received alloy wires were sent to the U.S. Testing Company, the Analytical Laboratory at Cornell University, and to the Reactor Laboratory at Michigan State University for chemical analysis. The results are shown in Table 3A. The designation by groups indicates independent tests on different pieces of wire. The MSU neutron activation results are the averages of tests from multiple samples. The values for the single samples are shown in Table 3B. The scatter in the test results from identical specimens indicates that they are accurate only to ± 10%.

Neutron activation analyses were done on portions taken from different parts along the as received alloy wires to check homogeneity. These tests were also performed on wires that had been drawn straight down to 5.0 mil diameter and on those that had been through the strainanneal process. These results are shown in Tables 3B and 3C. The alloy wires were found to be homogeneous, and there was no systematic loss of Co resulting from either the drawing or the strain-anneal procedure.

TABLE 3A.--Chemical Analyses.

	Wei	Weight Percent Co in Pt		
	A	В	С	D
Result 1				
Group 1		0.47 0.39	0.15 0.16	0.085 0.089
Group 2	1.14	0.55		
Result 2		0.525	0.171	0.087
Result 3				
Group 1		0.565	0.188	0.109
Group 2	1.176	0.461		
Average				
Weight %	1.16	0.50	0.17	0.094
Atomic %	3.74	1.65	0.56	0.31

Result 1: atomic absorption spectrography reported by United States Testing Co., Inc. 1415 Park Ave., Hoboken, N.J. 07030

Result 2: neutron activation analysis reported by Analytical Laboratory Material Science Center Cornell University

Result 3: neutron activation analysis reported by Reactor Laboratory Engineering Department Michigan State University

TABLE 3B. -- Test of Homogeneity.

Weight Percent Co in Pt	B C D	M E S M E S M	0.554 0.187 0.185 0.192 0.104 0.115 0.190	0.457 0.449 0.477 0.444
in Pt				
cent Co		S		
ight Per		臼		
Wei	В	M		0.457 0.477 0.477
		S	0.549 0.591	
	A	E		1.170 1.163 1.204
		M		1.172 1.170 1.176
70 L L &	ZOTTU .		Group 1	Group 2

On alloy wires as received at different places along the wire

S = starting end M = middle E = interior end

TABLE 3C.--Test of Strain-anneal Procedure.

		Weight P	ercent Co	in Pt
	as rec	ceived	drawn	strain-annealed
Alloy A	M 1.172 1.170 1.176	E 1.170 1.163 1.204	1.205 1.188 1.148	1.126 1.182
Alloy B	0.457 0.477 0.477	0.449 0.444 	0.447 0.447 	0.445 0.454

Portions of the pure Pt wire, the pure Pt wire that had been through the arc melting process, and the 0.3 at% PtCo alloy were sent to Schwarzkopf Microanalytical Laboratory for semiquantitative spectrographic analysis. Table 3D lists the elements that were found from among the thirty tested for. All the wires tested showed evidence of residual impurities. The reported cobalt content of the alloy agreed with that from other chemical analyses.

B. Control Specimens

Control runs are needed to establish which planes have sufficiently low artifact levels to be of practical use in alloy studies. For alloy systems such as PtCo, where both solute atoms and artifacts show up as vacant sites, control runs are critical. The concentration of artifacts should be as low as possible and at least within

TABLE 3D. -- Semi-quantitative Spectrographic Analysis.

	Pure Pt	Arc Melted Pt	PtCo Alloy
Aluminum	ND	ND	FT
Cobalt	ND	ND	${f T}{f H}$
Copper	ND	FT	${f TL}$
Iron	FT	ND	FT
Nickel	${f FT}$	FT	${f T}{f L}$

ND = not detected

FT = less than 0.01 weight percent

T = 0.01 to 0.1 weight percent

H = upper half of range shown

L = lower half of range shown

Reported by Schwarzkopf Microanalytical Laboratory 56-19 37th Avenue Woodside, N.Y. 11377

the uncertainty of the chemical analysis. This uncertainty in the present study is ten percent.

Two sets of control runs on pure Pt tips were made to measure background artifact levels. A field ion micrograph of a well-annealed Pt tip is shown in Figure 3A. One octant of the (001) oriented Pt tip is indexed.

As originally investigated by Speicher et al. (14) and later confirmed by Berger et al. (15) and Chen (13), a number of planes around the {102} plane show a low level of artifact vacant sites and good atomic resolution. The present investigation was consistent with those earlier results. The final total artifact and atom counts for the two sets of control runs are listed in

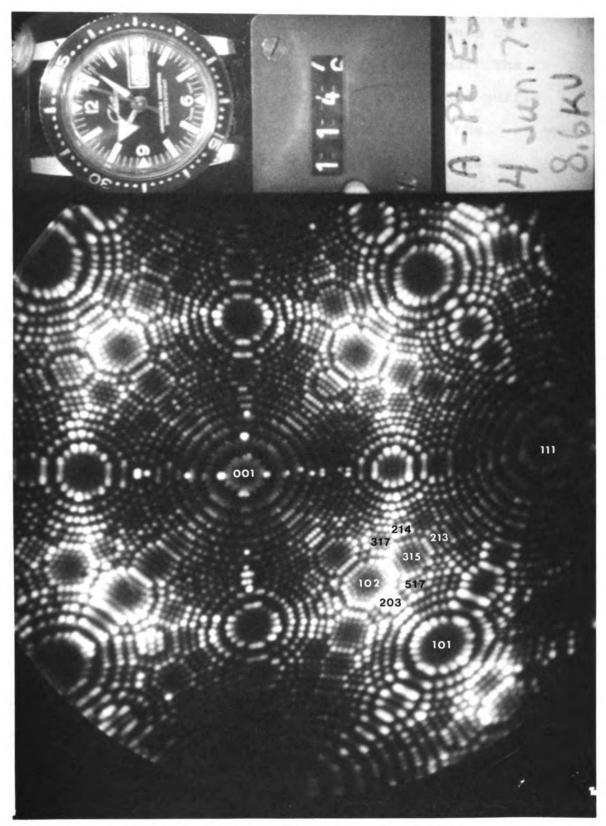


Figure 3A.--Field ion micrograph of pure platinum tip.

Tables 3E and 3F. α -dark spots are defined below in section C. The {102} and {317} planes had levels of artifacts too high for use in the alloy studies. The {315}, {213}, {203}, {517}, and {214} planes had sufficiently low artifact levels (less than 10% of the planned solute concentration). Other planes such as the {103} did not have adequate atomic resolution.

Set I of the controls was carried out with the system operating in a static pumping mode. The concentration of artifacts on the {315}, {213}, {203}, {517}, and {214} planes was less than five percent of the 0.6 at alloy, which was run under Set I conditions.

TABLE 3E.--Control Run Set I on Pure Platinum.

Plane	Number of atoms	Number of α-dark spots	Concentration of α -dark spots
{315}	20,775	1	4.8×10^{-5}
{203}	8,545	0	$<1.2 \times 10^{-4}$
{213}	18,255	0	$<5.5 \times 10^{-5}$
{517}	15,525	1	6.4×10^{-5}
{214}	10,700	2	1.9×10^{-4}
{317}	11,930	145	1.2×10^{-2}
{102}	10,860	189	1.7×10^{-2}

TABLE 3F.--Control Run Set 2 on Pure Platinum.

Plane	Number of atoms	α	β	Concentration of α-dark spots
{315}	11,530 7,670 7,600 26,800	31 8 13 52	6 0 0 6	$ \begin{array}{c} 2.7 \times 10^{-3} \\ 1.0 \times 10^{-3} \\ 1.7 \times 10^{-3} \\ \hline 1.9 \times 10^{-3} \end{array} $
{213}	8,910 4,410 3,420 16,740	4 23 0 27	0 3 <u>0</u> 3	$ \begin{array}{c} 4.5 \times 10^{-4} \\ 5.2 \times 10^{-3} \\ \\ \hline 1.6 \times 10^{-3} \end{array} $
{203}	2,140 2,400 4,410 8,950	5 0 <u>5</u> 10	3 0 <u>0</u> 3	$\begin{array}{c} 2.3 \times 10^{-3} \\ \\ 1.1 \times 10^{-3} \\ \hline 1.1 \times 10^{-3} \end{array}$
{517}	4,490 4,040 <u>4,395</u> * 12,925	0 5 19 ° 24	0 0 <u>3</u> 3	$\begin{array}{c} -2.5 \\ 1.2 \times 10^{-3} \\ 4.3 \times 10^{-3} \\ \hline 1.9 \times 10^{-3} \end{array}$
{214}	5,730 3,300 4,115 13,145	1 8 0 9	0 1 0 1	$ \begin{array}{c} 1.7 \times 10^{-4} \\ 2.4 \times 10^{-3} \\ \hline 6.9 \times 10^{-4} \end{array} $
{317}	7,630 4,220 6,420 18,270	174 85 95 354	0 3 <u>0</u> 3	$\begin{array}{c} 2.3 \times 10^{-2} \\ 2.0 \times 10^{-2} \\ 1.5 \times 10^{-2} \\ \hline 1.9 \times 10^{-2} \end{array}$
{102}	9,210 4,990 6,870 21,070	261 142 127 530	0 0 <u>1</u> 1	$ \begin{array}{c} 2.8 \times 10^{-2} \\ 2.8 \times 10^{-2} \\ \underline{1.8 \times 10^{-2}} \\ 2.5 \times 10^{-2} \end{array} $

^{*}One bright spot.

In an effort to upgrade the system, changes were made so that it could be operated in a dynamic pumping mode. Therefore, a second set of pure Pt specimens which had been through the same arc melting procedure as the alloy specimens were run. This second set of the controls had concentrations of artifacts over an order of magnitude higher than those of Set I.* Even with the higher level of artifacts, the background on the five better planes was less than 2 x 10⁻³. These background levels made practical the study of only the higher concentration alloys of 3.7 and 1.7 at%.

C. Alloy Specimens

Several different signatures were observed in the alloy specimens. The classification and designation of the various signatures used here is the same as that proposed by the Cornell group (16).

 $\alpha\text{-dark}$ spot: This is a single dark atomic site, lying within the outer ring, which is visible as soon as the layer above is removed.

 β -dark spot: In a layer where all the atoms can be seen, one atom may suddenly disappear leaving a single

It was later found that a small amount of air had gotten into the helium imaging gas for all the samples run under Set II conditions. A bulb of pure He gas is connected to the FIM system and the intervening space evacuated. The glass seal to the bulb is then normally broken by dropping a small metal rod incased in glass onto it. After the bulbful of He gas was exhausted, it was discovered that the glass casing on the metal rod had cracked allowing the trapped air to escape and contaminate the He gas.

dark spot. Once formed, it appears the same as an α -dark spot.

Bright spot: This is a single atomic site which appears much brighter than the nearby atoms.

The presence of the Co atoms caused a large number of α -dark and β -dark spots to be produced. The field dissection of a {315} plane in a 0.6 at% PtCo tip is shown in Figure 3B. In the schematics, an open circle represents an α -dark spot and an open circle with a cross represents a β -dark spot. The peeling of three successive layers is shown in frames 1-6, 7-10, and 11-16. One β -dark spot, appearing suddenly in frame 5, and one α -dark spot, frames 11-16, were found in these layers.

Images of the 0.6, 1.7 and 3.7 at% Co in Pt tips were recorded on film using our pulser control system. A field ion micrograph of a (111)oriented alloy tip is shown in Figure 3C. This alloy image is more irregular than the pure Pt image, in accord with the results of other experimenters.

After the films of the alloy tips were taken and processed, they were scanned using a Vanguard motion analyser. The various signatures were counted, the number of surface layers peeled through for each plane and an average number of atoms on each layer was recorded. This average was obtained by counting the actual number of atoms within the outer ring for three layers about the

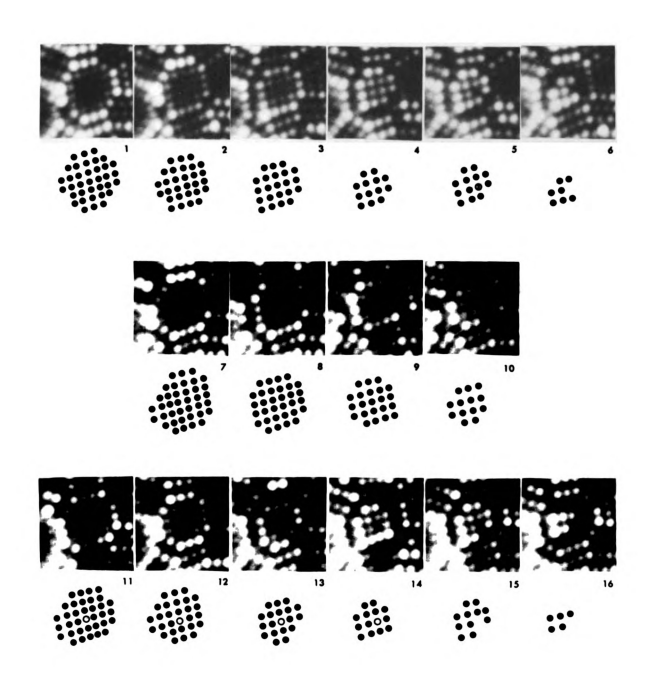


Figure 3B.--Field dissection of a {315} plane.

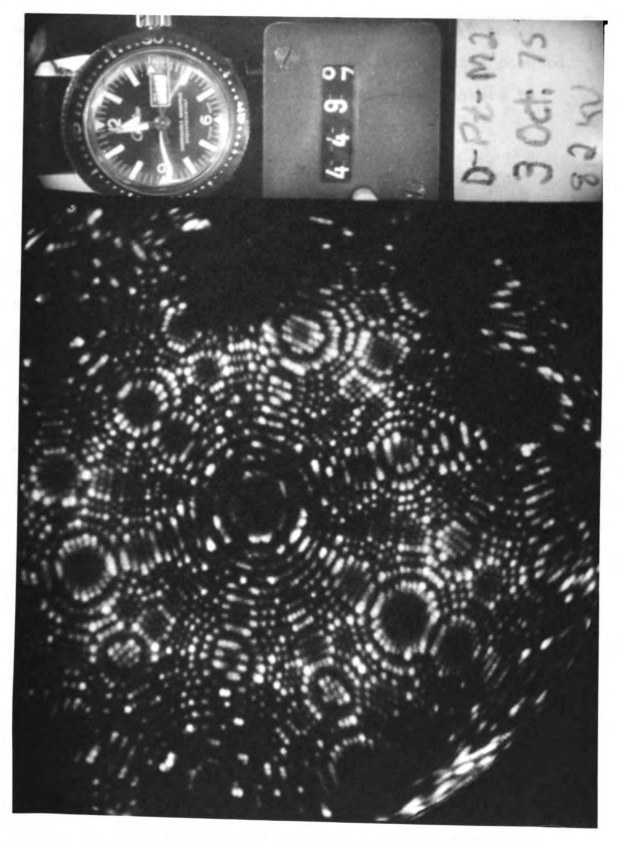


Figure 3C.--Field ion micrograph of a 3.7 at % PtCo tip.

median layer. As a check, the total number of atoms in all the layers of several planes was individually counted. The numbers obtained by the averaging method agreed to within ten percent of these actual counts.

1. The 0.6 at% Co in Pt Alloy

The α - and β -dark spots were counted in a number of planes for two 0.6 at% PtCo tips. The results are summarized in Table 3G. The experimental conditions for both runs on this alloy were the same as those for Set I of the controls.

TABLE 3G.--Results for 0.6 at% PtCo Alloy Tips.

Plane	Number of atoms	α	β	Concentration of α -dark spots
Tip 1				
{315} {213} {203} {517} {214} {317} {102}	14,825 12,040 3,670 5,595 4,280 6,840	93 101 22 31 43 270 238	40 55 0 18 13	0.63×10^{-2} 0.84×10^{-2} 0.60×10^{-2} 0.55×10^{-2} 1.00×10^{-2} 3.95×10^{-2} 3.95×10^{-2} 3.34×10^{-2}
Tip 2	7,130	236	U	3.34 X 10
{315} {213}	7,065 3,330	61 27	17 14	0.86×10^{-2} 0.81×10^{-2}
{317} {102}	4,070 3,910	179 164	1 0	4.40×10^{-2} 4.19×10^{-2}

On the control runs, there were five planes that had low background levels of artifacts, namely, the $\{315\}$, $\{213\}$, $\{203\}$, $\{517\}$, and $\{214\}$ planes. These levels are negligible compared to the alloy Co concentration, so no correction for artifacts was made. In the alloys, the $\{203\}$ and $\{517\}$ planes were found to have α -dark spot levels within the ten percent uncertainty of the chemical analysis. The $\{315\}$ and $\{213\}$ planes had slightly higher, and the $\{214\}$ plane a much higher concentration of α -dark spots.

2. The 1.7 and 3.7 at% Co in Pt Alloys

The α - and β -dark spots were counted for the 1.7 and 3.7 at% PtCo alloys, and these results are summarized in Tables 3H and 3J. The experimental conditions for the runs on both alloys were the same as those for Set II of the controls.

From the control run results presented earlier, the background level of artifacts to be expected in the alloy tips is known and can be subtracted. The corrected concentrations of α -dark spots are presented in Tables 3I and 3K. For the 1.7 at alloy, the {315}, {203}, and {517} planes had corrected values within fifteen percent of the known Co concentration. The {213} planes for this alloy were too faint to be counted. For the 3.7 at alloy, the {315}, {213}, and {517} planes had corrected

TABLE 3H.--Results for 1.7 at% PtCo Alloy Tips.

Plane	Number of atoms	α	β	Concentration of α -dark spots
Tip 1				
{315} {203} {517} {214}	9,340 2,330 3,535* 4,385	163 41 73 97	59 9 20 30	1.75×10^{-2} 1.76×10^{-2} 2.06×10^{-2} 2.21×10^{-2}
{317}	6,650	316	7	4.75×10^{-2}
Tip 2				
{315} {203} {517}	4,795 1,050 765	125 20 17	41 1 5	2.65×10^{-2} 1.90×10^{-2} 2.22×10^{-2}
{317} {102}	2,085 3,560	101 211	2 0	4.84×10^{-2} 5.93 x 10 ⁻²

^{*}One bright spot.

TABLE 3I.--Final Results for 1.7 at% PtCo Alloy Tips.

Plane	Total concentration of α-dark spots	Corrected for artifacts
{315}	2.04×10^{-2}	1.85 x 10 ⁻²
{203}	1.80×10^{-2}	1.69×10^{-2}
{517}	2.09×10^{-2}	1.90×10^{-2}
{214}	2.21×10^{-2}	2.14×10^{-2}

TABLE 3J.--Results for 3.7 at% PtCo Alloy Tips.

Plane	Number of atoms	α	β	Concentration of α -dark spots
Tip 1				
{315} {213} {203} {517} {214}	5,450 2,540 1,140 1,970 990	219 96 88 78 45	70 34 2 29 23	4.02×10^{-2} 3.78×10^{-2} 7.75×10^{-2} 3.95×10^{-2} 4.55×10^{-2}
{317}	2,750	238	4	8.65×10^{-2}
Tip 2				
{315} {213} {203} {517}	6,965 3,605 650 470	254 142 34 17	64 49 0 5	3.65×10^{-2} 3.94×10^{-2} 5.23×10^{-2} 3.62×10^{-2}
{317}	4,720	349	6	7.39×10^{-2}

TABLE 3K.--Final Results for 3.7 at% PtCo Alloy Tips.

Plane	Total concentration of α-dark spots	Corrected for artifacts
{315}	3.81×10^{-2}	3.62 x 10 ⁻²
{213}	3.87×10^{-2}	3.71×10^{-2}
{203}	6.82×10^{-2}	6.71×10^{-2}
{517}	3.89×10^{-2}	3.70×10^{-2}
{214}	4.55×10^{-2}	4.48×10^{-2}

levels of α -dark spots within five percent of the known Co concentration. The results for the {203} plane were nearly twice that of the other planes. For both alloys, the {214} plane again had a much higher concentration of α -dark spots.

D. Co Atom to α-dark Spot Correspondence

The concentration of α -dark spots for each of the three alloys varied from plane to plane. However, for each alloy, three of the five lower background planes had α -dark spot concentrations consistent with the known levels of Co atoms. Thus, the identification of a Co atom in Pt appearing as an α -dark spot, or a vacant site, can be made.

The $\{214\}$ plane in all three alloys had α -dark spot levels much larger than expected from a simple sum of the concentrations of Co sites and of known artifact sites. An examination of the number of α -dark spots on the higher background planes $\{102\}$ and $\{317\}$ shows that they also have this much higher concentration. Chen found for both Au and Ni in Pt that the $\{203\}$ planes generally had a slightly higher concentration of α -dark spots than the other planes (16). These additional α -dark spots may have been generated by the presence of solute atoms in the lattice and the resulting more irregular surface.

Fortunately, knowing the reason the cobalt atoms are imaged as vacant sites is not necessary for calculations of spatial distributions. Two alternative explanations have been suggested for the vacant sites (12). Either they could be unoccupied sites at which Co atoms have been selectively field evaporated, or they are sites which are not imaged because of a much smaller field ionization probability. Tsong and Muller (8, 9), based on their FIM images of ordered PtCo alloys, have argued for the latter. The much smaller field ionization probability, and hence the dark spot image would come from a slight electronic charge transfer to the Co atoms which would drastically reduce the local field strength above them.

The concentration of β -dark spots fluctuated greatly from plane to plane. These defects are caused by the sudden evaporation of an atom from the lattice, leaving a vacant site there (13, 16). The β -dark spots were found to be associated with the α -dark spots in one of two different ways. A number were found next to an α -dark spot on the same layer. Others, in accord with Chen's results, were found to be closely associated with an α -dark spot on the layer below.

CHAPTER IV

SPATIAL ANALYSIS

In order to determine the three-dimensional spatial distribution of solute atoms in an alloy it is necessary to reconstruct the series of surface layers. One needs to know the geometrical relationship among atoms on a given layer and also between successive layers. With the relative positions of solute atoms expressed in a common coordinate system, it is straightforward to compute the solute spatial distribution. This process is repetitious and so is best handled by computer. The computer program used in the present study is based on the one described by Chen (13).

A. Lattice Coordinates and Transformations

This section describes the procedures and transformations necessary to determine the positions of all the solutes in a common coordinate system. The process divides naturally into two parts. The first is a determination of the relative positions of the atoms on a given surface layer. The second is to correlate the positions of atoms on successive layers.



1. Relative Coordinates on One Layer

The following procedure is used to calculate the relative positions of all the atoms on a given planar layer.

It is first necessary to determine the geometry of the crystallographic plane. One good way to visualize and study the plane is to use a ball model. Such models for the {315} and {213} planes are shown in Figures 4A and The layer of dark balls on top represents the pattern that would be observed in a FIM image. This top layer can be schematically represented as in Figures 4B and 4D. From an arbitrary origin on each layer, two local planar vectors \overrightarrow{OA} and \overrightarrow{OB} can be chosen. These two vectors may be used to specify the position of any atomic site in the plane in terms of integral multiples of \overline{OA} and \overline{OB} , (M,N)respectively. In the {315} plane, for example, atom D has planar coordinates of (-1,2). The three-dimensional FCC coordinates of each atom relative to its planar origin can be specified by using the standard cartesian unit axis vectors (100), (010), (001). The coordinates of atoms A and B in the {315} plane in this coordinate system are (1.0, -0.5, -0.5) and (0.5, 1.0, -0.5), respectively.

The transformation between the two systems is straightforward. The local FCC coordinates (DX,DY,DZ) of

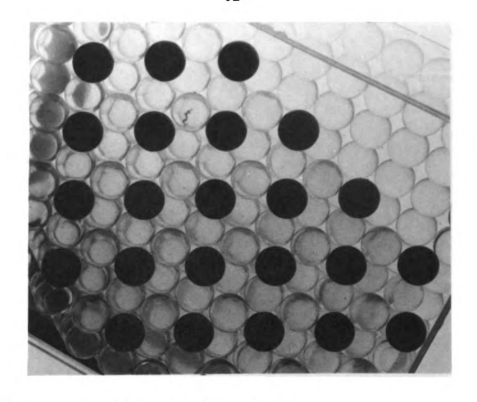


Figure 4A.--Ball model of {315} plane.

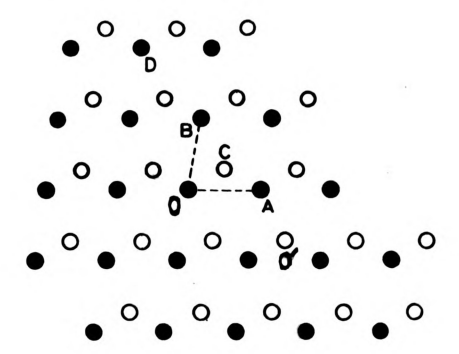


Figure 4B.--Schematic of {315} plane.

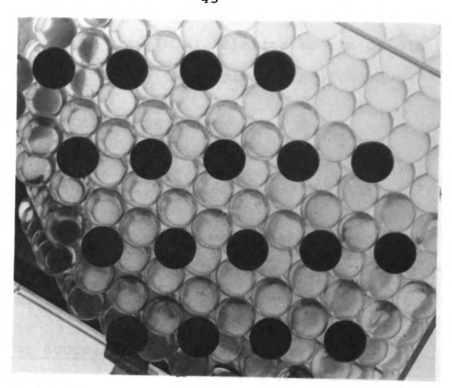


Figure 4C.--Ball model of {213} plane.

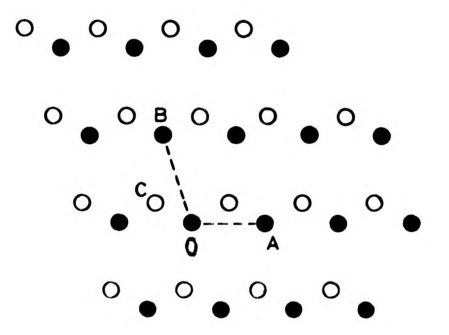


Figure 4D.--Schematic of {213} plane.

a planar coordinate site (M,N) relative to the origin site at (XO,YO,ZO) in any {315} plane are given by:

DX = XO + 1.0M + 0.5N

DY = YO - 0.5M + 1.0N

DZ = ZO - 0.5M - 0.5N

Using this transformation, the coordinates of all the atoms on a layer can be found in terms of the local FCC coordinate system.

2. Shift for Successive Layers

The next step is to determine the relative position of the origins of two successive layers. Once again, good use of the ball model can be made. When the top layer of atoms is removed, the new top layer of atoms consists of atoms that were first-nearest neighbors to the layer just removed. This shift can be specified either in terms of the local planar coordinate system or in terms of the local FCC coordinate system. The shift from the origin of the top layer to the one underneath it will probably not be to the particular atom that has arbitrarily been chosen as the origin of the lower layer. However, it is an easy matter to specify the integral shift necessary to move to the origin of the new top layer using the local planar coordinates described above. Once the shift between the two origins is known, the relative positions of any pair of atoms on the two layers can be readily calculated. A detailed account of the shifts between layers and the associated computer program is given in Appendix A.

3. Nonideal Image

In an ideal lattice, the shift from layer to layer is always a uniform distance from an atomic site to a first nearest neighbor site. In practice, this shift does not turn out to be so regular. The lattice is still perfect; however, there are slight deviations in the image. The images of the edge atoms are often larger. Also the rows or columns may be slightly curved or have unequal spacings.

A simple computer program cannot always cope with distortions of the lattice images. Sometimes it is necessary to plot out all the atoms of several successive layers and examine them by eye to get the correct shifts from layer to layer. For example, if the shift between the first and second layer is smaller than usual, then in most cases the shift between the second and third is larger, so the net effect will be an average shift that is as expected of the crystal lattice.

B. Radial Distribution Function

1. Definitions

One useful way of presenting the spatial distribution is as a radial distribution function, that is, the

average number of solute atoms around a given solute atom as a function of their radial distance. It is especially useful when normalized to the case of a random distribution. The normalized radial distribution function immediately shows any tendency of the system towards clustering or short range order.

Following Chen (13, 16) the radial distribution function is defined as:

$$R(r_i) = \frac{2 Np_i}{N_s}$$

where $R(r_i)$ is the average number of solute atoms at distance r_i around a solute atom,

i indexes the ith nearest neighbor shell,

 ${\rm Np}_{\tt i}$ is the number of ith nearest neighbor solute atom pairs, and

 $\rm N_{\rm S}$ is the number of solute atoms, all in a given fixed volume.

Normalizing this distribution to a random distribution permits ready identification of clustering or short range order. For the case of a random distribution:

$$Np_i = \frac{N_s c Z_i}{2}$$

where c is the concentration of solute atoms, and Z; is the coordination number of the ith shell. This leads to:

$$R_{random}(r_i) = c Z_i$$

The normalized radial distribution function (NRDF) or ratio is:

$$\frac{R(r_i)}{R_{random}(r_i)} = \frac{2 Np_i}{N_s c Z_i}$$

At a given distance r_i , this ratio is the ratio of the observed number of ith nearest neighbor pairs compared to what one would expect for a random distribution. distribution were random, then the NRDF or ratio will be one for all nearest neighbor shells. The first eight to ten nearest neighbor shells of a radial distribution function are the most important, since possible interactions between solute atoms are stronger at close distances. Also, in these alloys, with a few percent solute atoms, there is no long range order. The degree of short range order is of interest, and this will show up on the nearest neighbor shells. At further distances, because of the long range disorder, the distribution will average to random. So for all types of spatial distributions the ratio should approach one for farther neighbor shells.

2. Types of Spatial Distributions

The types of spatial distributions described here are for dilute alloys with no long range order. There are three basic types: random, clustering, and ordering. As mentioned above, a random distribution will have a ratio equal to one for all nearest neighbor shells. Clustering manifests itself by the ratio being greater than one for the first few nearest neighbors and dropping off to one at more distant nearest neighbors. The presence of short range ordering is seen in the ratio being less than one for the first few nearest neighbors, then rising to above one in the midrange before dropping off to one at farther nearest neighbor distances. These cases are illustrated in Figures 4E and 4F.

Radial distribution function analyses for Au and Ni in Pt were calculated by Chen (16). The dilute PtAu results showed definite evidence of clustering with patterns similar to that in Figure 4E. The dilute PtNi alloy result was consistent with short range order with a pattern similar to that in Figure 4F.

Schwerdtfeger and Muan (18, 27) have made activity measurements on both PtNi and PtCo. These measurements were made on concentrated alloys (10% Ni and Co, and higher) at equilibrium temperatures of 1270-1470°K for Ni and 1470-1670°K for Co. Chen has estimated a freeze-in temperature of 1100°K for his PtNi alloy, and

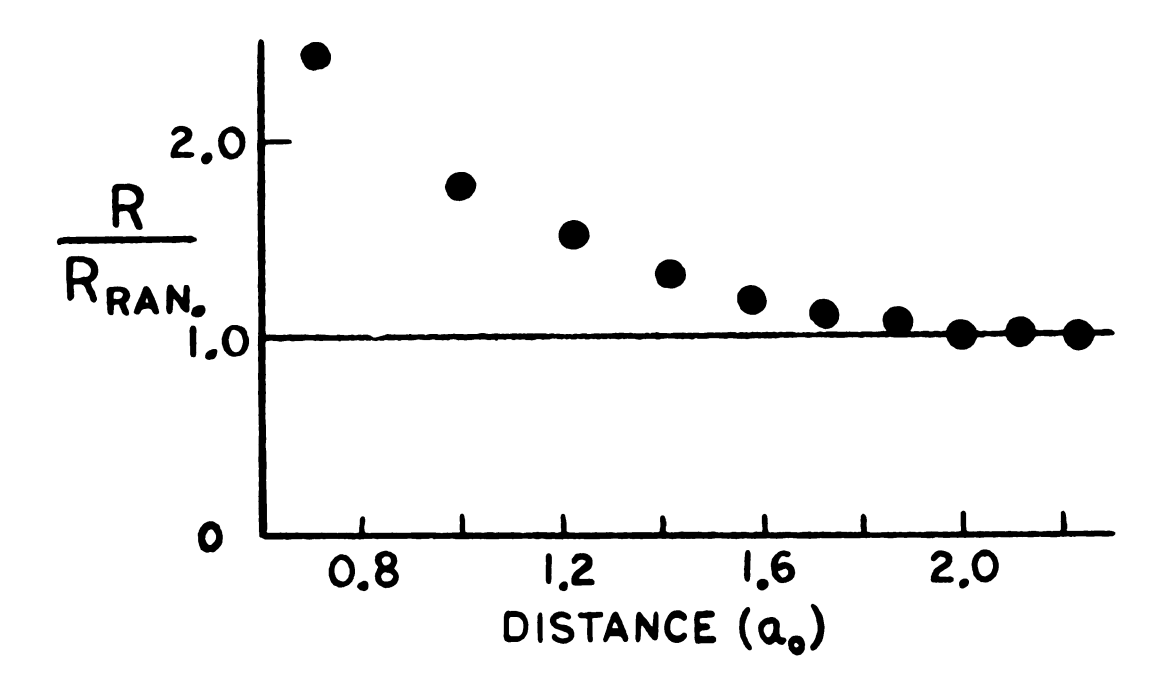


Figure 4E.--Pattern for clustering.

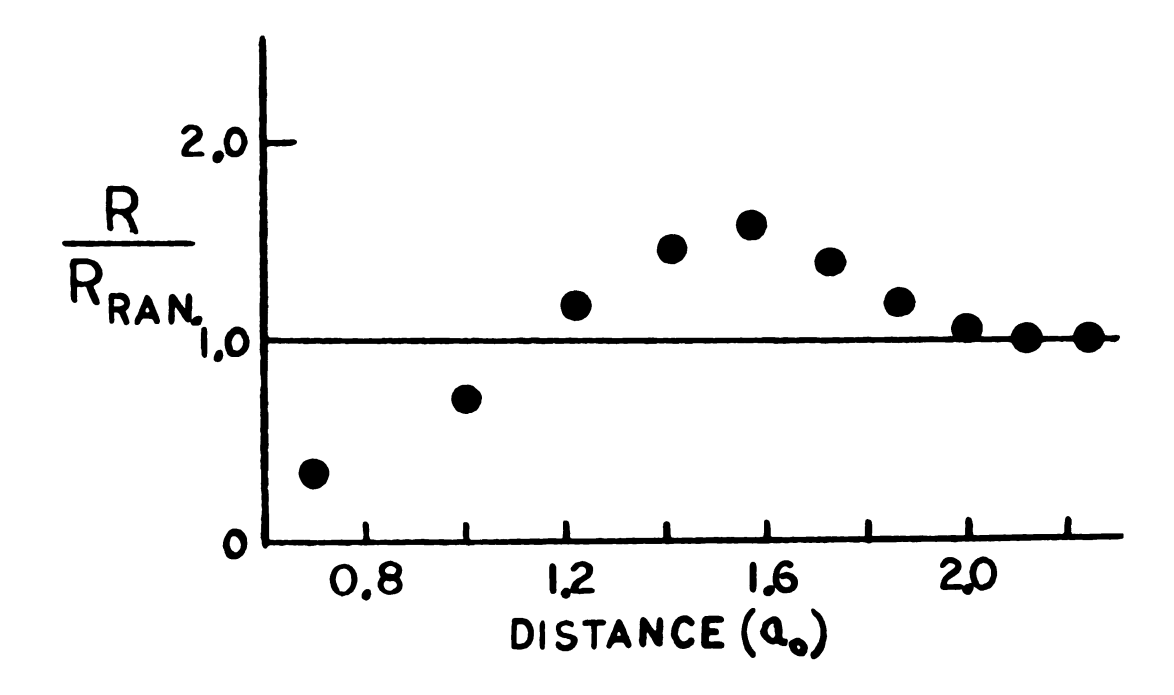
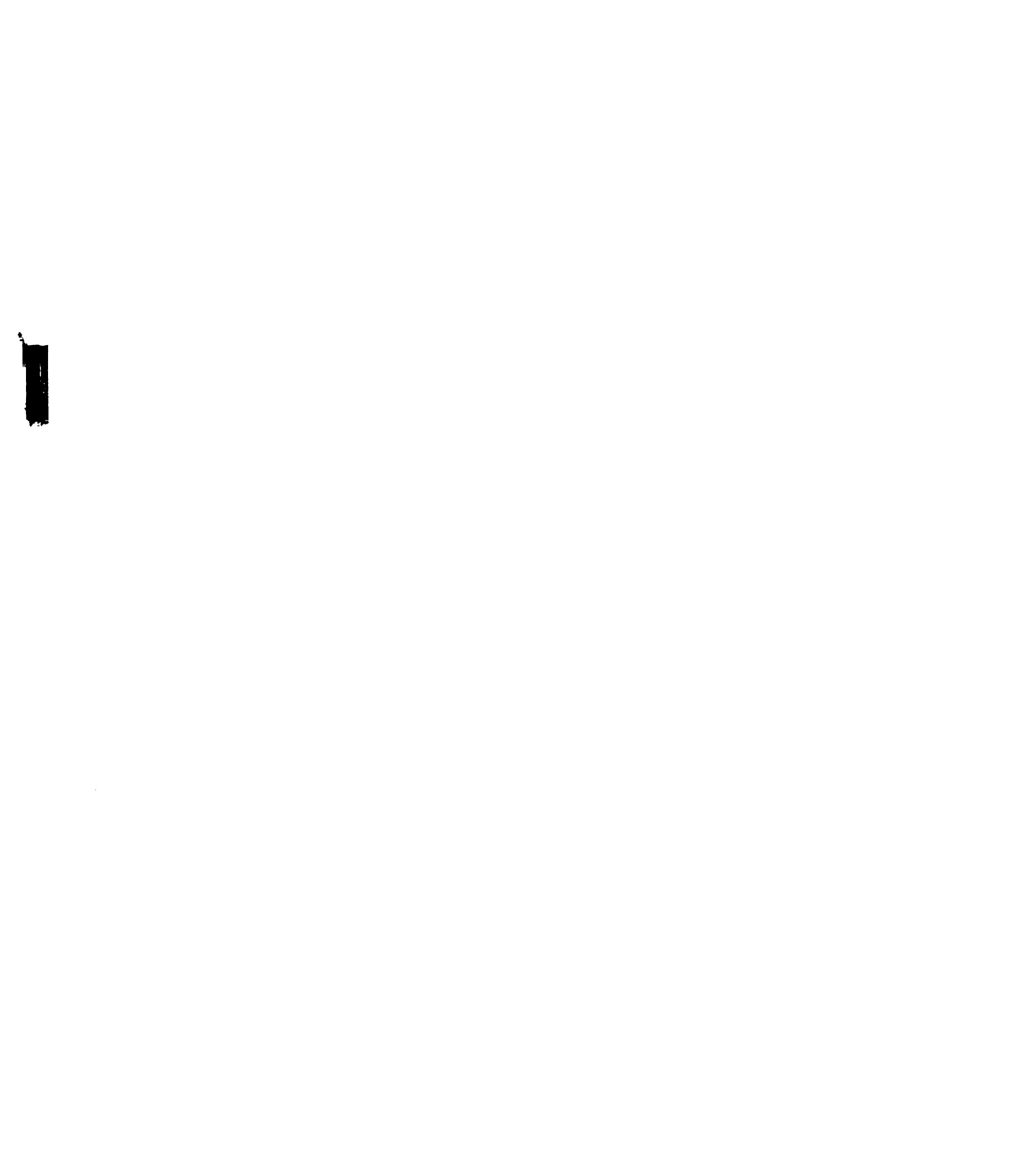


Figure 4F.--Pattern for short range order.



in the present study, an effective temperature of 1000°K was calculated in Chapter II. These temperatures are not much lower than those for the activity experiments. The results of the activity measurements show that Co in Pt has a stronger short range ordering tendency than does Ni. However, for both Ni and Co, the alloys should become more nearly random as they become more dilute.

Since Chen, with an examination of 320 solute sites on a dilute 0.6 at% alloy, inferred short range order for Ni, it should be necessary to examine only a few hundred Co sites of a more concentrated alloy, 3.7 at% PtCo, to determine if it has the expected greater ordering tendency. Additionally, an estimate of the ratio of first nearest neighbor pairs to be expected for PtCo can be made using the x-ray scattering results of Rudman and Averbach (19). Using their extrapolation of the local order parameter α_1 to the lower concentration of 3.7 at%, one gets α_1 = -0.02. The normalized ratio for the first nearest neighbor is related to α_1 as follows:

$$\frac{R_1}{R_{ran}} = 1 + \frac{\alpha_1(1-c)}{c} ,$$

where c is the concentration of Co. This relation yields a value of $\frac{R_1}{R_{ran.}}$ = 0.5 which should be observable.

3. Correction for Coordination Numbers

Since the volume examined by the FIM is finite, the coordination numbers, Z_i , must be corrected from those normally associated with an infinite crystal. This correction turns out to be sizeable because of the large surface to volume ratio of the planes examined. The surface atoms have many fewer ith nearest neighbors, resulting in a decreased average coordination number. An effective coordination number can be obtained by studying a typical FIM plane.

To obtain these averaged effective $\mathbf{Z_i}$'s for a given crystallographic plane, the coordinates of all the atoms in a typical plane are fed into a computer program. This program calculates the coordination numbers for each atom and then averages over all atoms to get the effective average coordination number $\overline{\mathbf{Z}_i}$. These $\overline{\mathbf{Z}_i}$ are given in Table 4A. For both the {315} and {213} planes, these $\overline{\mathbf{Z}_i}$ are systematically lower than those found by Chen (16). This is presumably due to there being fewer atoms on each layer of the planes in the present study.

C. Data and Results

1. The 3.7 at% PtCo Alloy

The number of nearest neighbor pairs was calculated out to the tenth nearest neighbors for the 3.7 at%

PtCo alloy. A total of 12965 atomic sites containing 517

TABLE 4A. -- Average Effective Coordination Numbers.

	{315}	{213}	Infinite Crystal
\mathbf{z}_{1}	8.5	7.9	12
z_2	3.9	3.6	6
z ₃	15.1	14.0	24
z ₄	7.0	6.5	12
z ₅	13.2	12.3	24
z ₆	4.2	4.0	8
z ₇	24.1	22.2	48
z ₈	2.8	2.6	6
z ₉	16.2	14.9	36
z ₁₀	10.4	9.5	24

vacant sites from two different tips and two different planes, the {315} and {213}, were examined. The results are presented in Table 4B.

2. Correction for Artifacts

The effect of the artifact background was checked by examining the α -dark spots of some typical {315} planes in a well annealed pure Pt tip. As was suspected from the initial viewing of the film, the artifact vacant sites occurred in small clusters of two to five atoms. The results are shown in Table 4C. These clusters are very localized with the atoms in each being mainly first, second, or third nearest neighbors of each other. An average effective background distribution has been

TABLE 4B.--Number of ith Nearest Neighbor Pairs in 3.7 at% PtCo.

1	2	m	4	വ	9	7	8	6	10
	23	48	36	47	13	100	10	09	44
	18	41	37	51	ស	73	6	51	43
	12	32	26	37	12	99	ω	54	42

TABLE 4C. -- Artifact Nearest Neighbor Pairs in Pure Pt.

{315} plane	Number of Artifacts	Number of i th pairs					Visual Cluster
prane	Artifacts	1	2	3	4	5	Cluster
1	2	8	1	1	_	_	4
2	6	2	-	-	-	-	3,2
3	6	-	-	_	-	-	
4	2	-	-	-	-	-	
5	0	-	-	-	-	-	
6	1	-	-	-	-	-	
7	7	10	3	6	1	1	5
8	7	9	1	1			5,2
Average 10,000 a	atom	17.7	3.0	4.9	0.6	0.6	

calculated. This gives the number of first, second, and third nearest neighbor pairs per unit 10,000 atom volume to be expected from artifacts. These numbers can be scaled so that the total number of atoms matches the number of atoms in the alloy volume. Then the number of first, second, and third nearest neighbor pairs can be subtracted from the alloy counts of nearest neighbor pairs.

D. Discussion

The normalized radial distribution function is easily calculated once the number of nearest neighbor pairs is known. These normalized ratios, corrected for

artifacts are plotted as circles in Figure 4G. The error bars associated with each ith nearest neighbor value is one standard deviation, σ , determined in the following manner. The standard deviations for the three planes were combined using

$$\frac{1}{\sigma^2} = \frac{1}{\sigma_a^2} + \frac{1}{\sigma_b^2} + \frac{1}{\sigma_c^2}.$$

For each of the three planes, one standard deviation, σ_{i} , is proportional to the square root of the number of counts of the ith nearest neighbor pairs. Given the uncertainties, the ratios are generally consistent with one at all distances. This is indicative of a random distribution. The uncorrected ratios, which differ only for the first, second, and third nearest neighbors, are plotted as crosses. These ratios are higher, but still consistent with a value of one. To establish a lower bound on the first nearest neighbor value, one can assume that all the extra concentration of \alpha-dark spots above the Co concentration are artifacts and subtract them from the distribution. This lower bound gives a value of 1.0 for the first nearest neighbor, consistent with a random Thus no evidence is found for the short distribution. range order suggested by the measurements of Rudman and Averbach (19) or Schwerdtfeger and Muan (18, 27). This is the opposite of the result recently found by Chen (16),

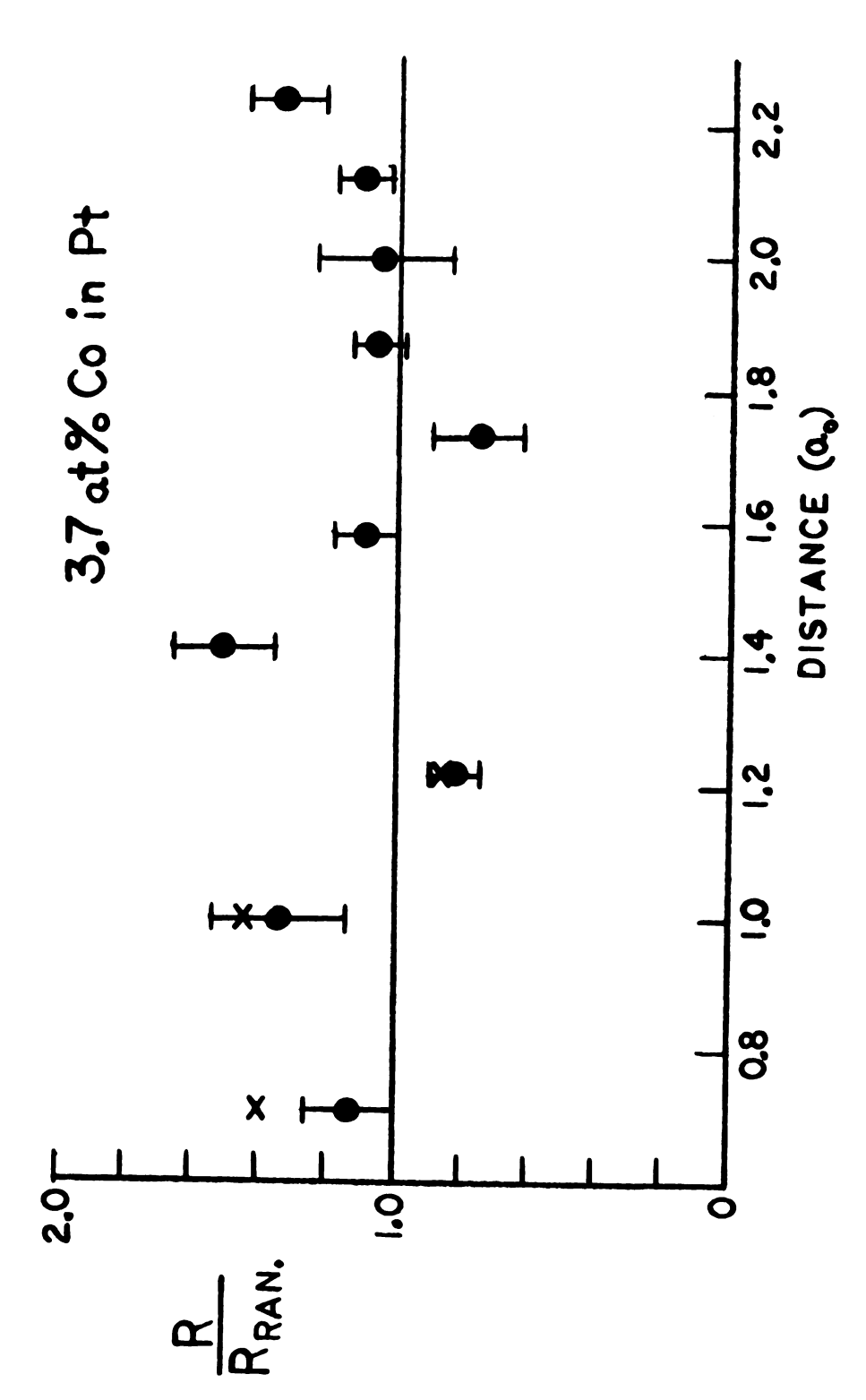


Figure 4G.--Normalized radial distribution function.

who reported observing the ordering in PtNi. This is somewhat surprising, since according to Schwerdtfeger and Muan, PtCo orders more strongly than PtNi. Moreover, since the present study involved the examination of a greater number of sites on a more concentrated alloy than the PtNi work, an ordering comparable to that reported by Chen should have been observable.

PART II

TRANSPORT MEASUREMENTS ON HIGH PURITY TUNGSTEN AT LOW AND ULTRA-LOW TEMPERATURES

The second portion of this thesis is a report of transport measurements on high purity single crystal tungsten at low and ultra-low temperatures. Three groups of experiments are described: size dependent electrical resistivity measurements on thin wires at 4.0°K; determinations of electric resistivity on 1.4 mm diameter rods below 1°K; and thermoelectric ratio measurements on the same rods, also at ultra-low temperatures. These three sets of experiments will be discussed individually in the following chapters.

CHAPTER V

SIZE DEPENDENT ELECTRICAL RESISTIVITY IN TUNGSTEN

A. Introduction

One means of studying the scattering of conduction electrons at the surface of a metal is by measuring the size dependence of the resistivity of thin wires. As wires are thinned down to where the electron mean-freepath becomes comparable to the sample diameter, the resistivity increases due to surface scattering. classical size-effect regime is where the electron meanfree-path ℓ is larger than the wire diameter d and much larger than the electron wavelength. The usual theoretical treatments (28,29) assume that the surface scattering is a mixture of diffuse and specular scattering. Diffuse scattering occurs when the incident electron has an equal probability of being scattered into any electronic state. Specular scattering occurs when the component of the wave vector parallel to the surface is conserved. Diffuse scattering contributes to electrical resistivity while specular scattering does not.

Size dependent electrical resistivity measurements on single crystal tungsten have been made by several

groups (30, 31, 32). Almost all of the data were taken on samples with diameters greater than 0.1 mm, and were found to be consistent with completely diffuse scattering, except for the data of Baer and Wagner (30). They altered the condition of the surfaces of their wires and found reversible changes in the resistivity, implying variations in the nature of the surface scattering. The data of the present study are for thinner well-annealed single crystal samples. Thus, at 4.2°K, the electron mean-free-paths are very much greater than the sample diameters. It was found that these wires had resistivities considerably smaller than would have been expected from the published information on tungsten (30, 31, 32). In terms of the usual treatment of surface scattering in thin wires, these resistivities can be understood only if surface scattering in tungsten is substantially specular instead of completely diffuse.

The rest of this chapter consists of three parts. First, the Nordheim model of the resistivity of a thin wire is generalized to allow for an anisotropic electron mean-free-path, and then used to derive a lower bound for the resistivity of a wire when the surface scattering is completely diffuse. Secondly, sample preparation is discussed. Then the data are presented and shown to fall below the lower bound previously derived. The implications of this result for specular scattering are then considered.

B. Theory

The resistivities of thin wires are almost invariably found to increase linearly with the inverse of the wire diameter (28, 29). The simplest explanation for this behavior is provided by the Nordheim equation (28).

$$\rho(d) = \rho_b + \alpha \frac{\rho_b \ell_b}{d}.$$
 5.1

Here $\rho(d)$ is the measured resistivity of a wire of diameter d, ρ_b is the resistivity of the same material in bulk form, ℓ_b is the electron mean-free-path averaged over the Fermi surface, and α is a parameter which specifies the amount of specular reflection at the sample surface. For completely specular scattering, $\alpha=0$; for completely diffuse scattering, $\alpha=1$. α is related to the standard "specularity parameter" p (28, 29) through the equation

$$\alpha = \frac{1 - p}{1 + p}.$$

For a metal with an isotropic electron mean-freepath, Equation 5.1 can be rewritten in terms of the total Fermi surface area S of the metal of interest as (29):

$$\rho(d) = \rho_b + \frac{\alpha e^2}{12\pi^3 hSd}$$
 5.3

Equation 5.3 would not be expected to apply to tungsten, which has a complicated Fermi surface and therefore probably an anisotropic electron mean-free-path. However, following Olsen (28, 33) Equation 5.3 can be used as the basis for a derivation of $\rho(d)$ in which anisotropy is explicitly taken in account. The Fermi surface of the metal is divided into regions S_j each of which is small enough to have an isotropic mean-free-path, and then Equation 5.3 is applied to each of these regions.

That is, it is assumed that

$$1/\rho = \Sigma_{j} 1/\rho_{j}, \qquad 5.4$$

where

$$\rho_{j} = \rho_{jb} + \alpha \frac{\rho_{jb}^{l}jb}{d} = \rho_{jb} + \frac{\alpha e^{2}}{12\pi^{3}hs_{j}d}.$$
 5.5

Here S_j is chosen so small that ℓ_{jb} is isotropic over S_j , and α is assumed to be isotropic over S_i .

Combining Equations 5.4 and 5.5 one obtains

$$1/\rho(d) = \sum_{j [\rho_{jb} + \frac{\alpha e^2}{12\pi^3 \hbar s_j d}]} 5.6$$

A lower bound to $\rho(d)$ can be obtained by merely setting all the ρ_{jb} = 0 in which case Equation 5.6 reduces to

$$\rho_{L.B.}^{(d)} = \frac{\alpha e^2}{12\pi^3 h S d} \le \rho(d)$$
5.7

This is a lower bound to Equation 5.6, because all of the quantities which have been omitted are positive and appear only in the denominators of the terms on the right-hand side of Equation 5.6. Therefore, omitting these quantities can only decrease ρ . Comparison of Equation 5.6 with Equation 5.7 shows that $\rho(d)$ becomes equal to its lower bound only in the very thin wire limit when $d \ll \ell_j$ for all ℓ_j . This result is physically plausible, since in this limit essentially all of the electrons have the "isotropic" mean-free-path d, and thus one would expect to obtain the thin wire limit of Equation 5.3.

Within the framework of the Nordheim equation (Equation 5.1) generalized to the "multi-band" model for ρ (Equations 5.4 and 5.5), Equation 5.7 must represent an absolute lower bound on $\rho(d)$. If $\alpha=1$, then $\rho(d)$ cannot be smaller than $e^2/12\pi^3\hbar Sd$. Conversely, if $\rho(d)$ is found experimentally to be smaller than $e^2/12\pi^3\hbar Sd$, then one is forced to conclude that $\alpha<1$.

For tungsten, the value of S has been determined from measurements of the de Haas-van Alphen effect to be (34, 35) S \approx 16.5 Å⁻². For α = 1, putting this value into Equation 5.7 yields

$$\rho_{L,B}^{(d)} = \frac{9.2 \times 10^{-12} \Omega - cm^2}{d(cm)}.$$
 5.8

The results of the present study will be compared with Equation 5.8.

C. Samples

The single crystal wires used in this investigation came from three different sources. A wire of diameter 61 μ , having unknown orientation, was zone-refined and electropolished to size by J. Galligan, then at Brookhaven National Laboratory. A second wire of diameter 62 μ , oriented with its axis along the (112) crystallographic axis, was zone-refined by B. Addis at Cornell University and electropolished to size in our laboratory. Three additional wires having diameters 28 μ , 41 μ , and 48 μ were three-pass zone-refiend (base pressure < 5 x 10⁻⁸ mm Hg) and electropolished to size in our laboratory. These wires were not oriented directly along crystallographic axes, but all lay between 10° and 15° from (100). All five wires had bulk Residual Resistance Ratios (RRR = $R_{273\,\text{K}}/R_{4.2\,\text{K}}$) exceeding 30,000.

The sample gauge lengths were determined by 8 μ tungsten wires spotwelded to the samples. To remove any cold-work introduced by the spotwelding, the samples were annealed at temperatures greater than 3000K before being measured.

The sample diameters were calculated from measurements of sample length and sample resistance at 273K, using $\rho(273K) = 4.9 \times 10^{-6} \ \Omega$ -cm (36) as the resistivity of pure tungsten at 273K. The average diameters should therefore be reliable to a few percent. As a check against gross error, these diameters were verified by visual comparison with drawn wires of known diameter. Care was taken to make the samples as uniform in thickness as possible, since they were heated for annealing by passing a current through them, and substantial non-uniformities in thickness would cause them to burn through. The estimated thickness variation along a given specimen is less than 10%.

D. Experimental Data and Analysis

In Figure 5A the inverse RRRs of the samples are plotted as a function of their inverse diameters. This is equivalent to a plot of sample resistivity versus inverse diameter, since, neglecting the thermal contraction of less than 1% which occurs as the sample cools form 273K to 4.2K, the resistivity at 4.2K can be written as

$$\rho (4.2K) = \frac{\rho (273K)}{RRR}$$
 . 5.9

The present data are the filled circles. For comparison, data obtained by other investigators is included; the

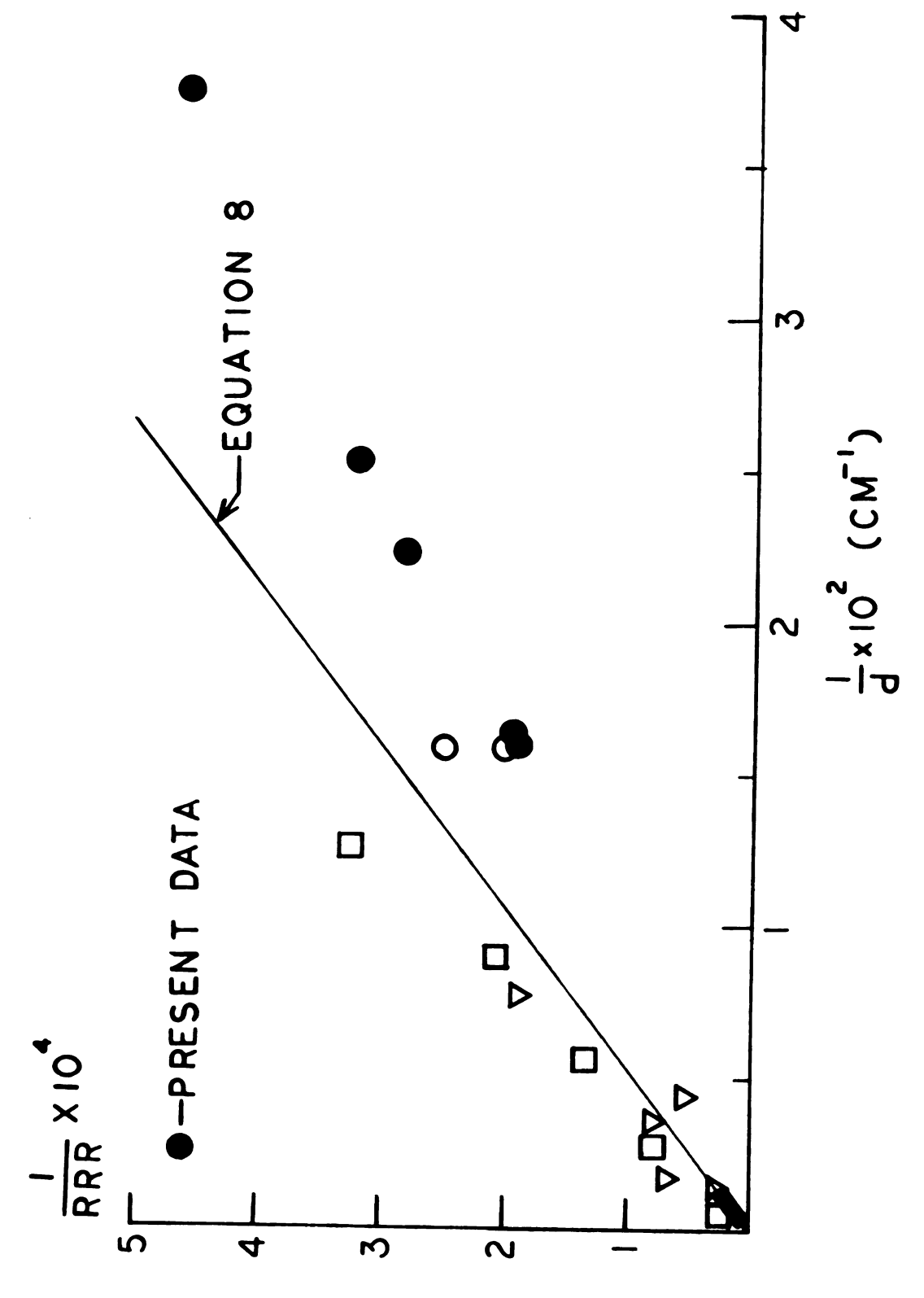
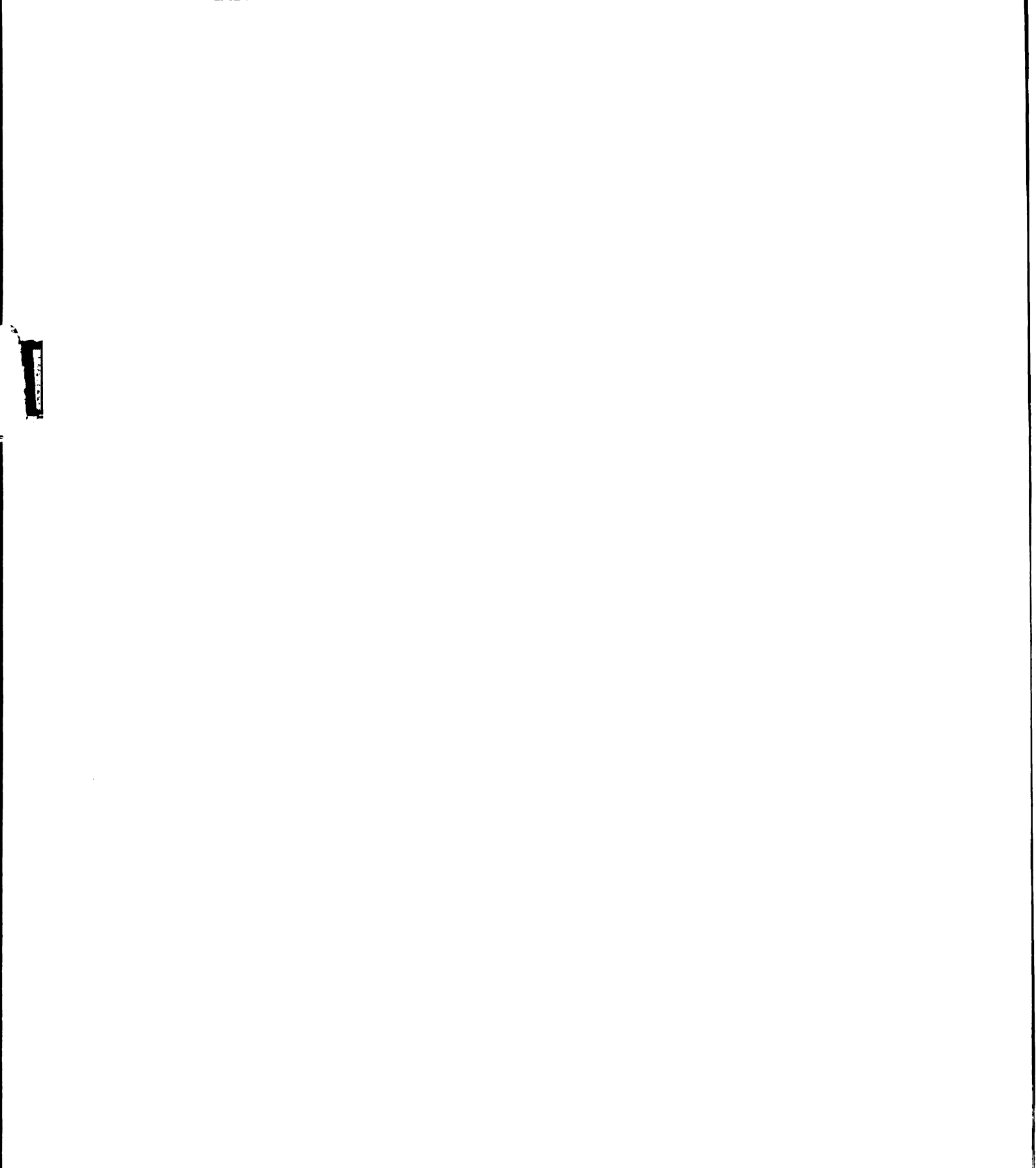


Figure 5A. -- Inverse RRR's of tungsten wires.



open circles are the data of Park et al. (37), the open triangles are the data of Baer and Wagner (30), the open squares are the data of Startsev et al. (32) and the solid bar indicates the data of Dausinger (31).

Most of the data in Figure 5A fall above the solid line which represents Equation 5.8, the lower limit to $\rho(d)$ for $\alpha = 1$. However, the data of the present study as well as two points recently obtained by Park et al. (37) and one point obtained by Baer and Wagner (30) fall below this line.

In view of the fact that the resistivities in the present study are smaller than would have been expected for diffuse surface scattering, the data were examined for systematic errors which would have caused the measured resistivities to be too small. Cold-work or impurities introduced during thinning would only increase the resistivities for a given sample diameter. So would nonuniformities in sample diameter. Uncertainties in the magnitude of the sample diameter large enough to move the data to the left far enough to reach the solid line were eliminated by the visual comparison noted above. Deviations from Ohm's law were checked for by varying the sample current, and no significant changes in sample resistance were observed. Current jetting was checked for by attaching four potential leads to some thin tungsten samples, two on one side of the sample diameter and two

on the other. The resulting resistances were internally consistent, independent of whether the pair of potential leads used were on the same or opposite sides of the wire.

No systematic errors could be found which would account for the data falling so far below the solid line in Figure 5A. Therefore, based upon the analysis given above, the surface scattering in the tungsten wires of the present study cannot be completely diffuse. Drawing a line from the origin through the data points of the present study yields a value of $\alpha \lesssim 0.7$. This corresponds to a specularity parameter of p $\gtrsim 0.2$.

CHAPTER VI

ELECTRICAL RESISTIVITY MEASUREMENTS IN TUNGSTEN AT ULTRA-LOW TEMPERATURES

A. Introduction

There has been considerable interest in the mechanism which determines the temperature dependent portion of the electrical resistivity of transition metals at low temperatures. Various studies have revealed a dominant T² component for the electrical resistivity (38,39,40,41,42,43,44). This T^2 behavior is now generally attributed to electron-electron scattering on the Fermi surface, in which s-electrons are scattered by d-electrons (45, 46). Of all the transition metals, tungsten has the smallest electronic specific heat (47), and thus the smallest number of d-states at the Fermi energy. With only a small number of d-states to scatter from, electron-electron scattering should only be a small portion of the electrical resistivity ρ . The T² component is so small in tungsten that prior to the present study a pure T2 variation had not been observed, even in the most recent investigations which extended down to about 1.3°K (44, 48). In these investigations, data were analyzed by

assuming that

$$\rho = \rho_{O} + AT^{2} + BT^{5},$$
 6.1

where each of these terms is identified with a unique contribution to the electrical resistivity ρ . The constant term ρ_0 arises from electron-impurity scattering. As mentioned above, the T² term is assigned to electron-electron scattering. The T⁵ term represents an attempt to account for effects of electron-phonon scattering. The problem with this equation is that the validity of this last term has not been established experimentally for tungsten. If it is not correct, then the use of the equation will yield spurious values for ρ_0 and A. The only sure way to confirm the existence of a T² component and to determine ρ_0 and A precisely is to go to temperatures so low that any higher order terms are negligible.

Recently, Wagner (49), based on new measurements on tungsten, questioned whether the very low temperature T² variation of the resistivity of tungsten is dominated by electron-electron scattering. He measured the high field magnetoresistance of tungsten between 1.4 and 4.2°K and concluded that his measurements could not be understood in terms of electron-electron scattering. Instead, he attributed them to electron-phonon scattering involving Umklapp processes. Extending his reasoning, he suggested that electron-phonon Umklapp scattering might also be the

source of the apparent T² term in the zero field resistivity. Recent calculations of impurity dominated electrical resistivity have indicated that in metals having complex Fermi surfaces, electron-phonon Umklapp scattering can produce resistivities varying approximately at T² over a narrow temperature range (50, 51). However, at still lower temperatures, Umklapp scattering should "freeze out," and the resistivity should then decrease more rapidly than T².

Wagner's suggestion, combined with these theoretical results, provided the stimulation for measuring the resistivity of high purity tungsten at temperatures well below 1°K in order to determine if ρ decreases more rapidly than T^2 . In this chapter, the results of these measurements are described. It is shown that to within the measuring uncertainty of about 1 part in 10^4 the resistance of high purity tungsten is consistent in the equation

$$R = R_0 + CT^2$$

down to at least 75 mK, as would be expected for electron-electron scattering. No evidence was found of the more rapid decrease which would be predicted for electron-phonon Umklapp scattering.

B. Experimental Procedure

The resistances of two zone-refined single crystals were measured: sample W-1 having a Residual Resistance Ratio [RRR = R(299K)/R(OK)] of 44,000 and sample W-3 having RRR = 22,000. Both samples had gauge lengths of about 2.3 cm, determined by superconducting potential leads. These leads were soft soldered to platinum foils which had been spotwelded to the samples. A known resistance (R = 3.59 x 10^{-7} Ω) was connected in parallel with the sample via the potential leads, one of which was magnetically coupled to a SQUID null detector. The electrical resistance R of the sample was measured by adjusting the currents through the sample and known resistance until the potential differences across them were the same. For a 3-second time constant, the noise in the system was approximately $2 \times 10^{-15} \text{V}$, comparable with the Johnson noise in the known resistor which was held at 4.2K. To keep the self-magnetic field of the sample from affecting R, the current through the sample was limited to 40 ma or less. Measurements with currents differing in magnitude by a factor of two were the same to within the measuring uncertainty. The currents through both the sample and the known resistor were passed through precision resistors (10Ω , 100Ω , or $1k\Omega$), and the resulting potential differences were measured to five places using DVMs. Checks were made to ensure that the

DVM readings, the various resistors in the system, etc., were constant and/or reproducible to a few parts in 10^5 over the several hours involved in a set of measurements. Although R was determined to better than 1 part in 10^4 relative to the known resistance, the absolute uncertainty in ρ was limited to a few percent by the uncertainty in the geometric factor (length/area) of each sample.

The sample was cooled with the home-build dilution refrigerator described in a Ph.D. thesis by Imes (52). The temperature of the sample was determined using a Cryocal CR-50 doped germanium resistance thermometer which was calibrated against a powdered CMN thermometer over the entire temperature range. The accuracy of this calibration was tested above 1K by direct comparison with an independent Scientific Instruments SIN2G germanium resistance thermometer which had been purchased calibrated. Agreement between the two sets of data suggested that the doped germanium thermometer should be accurate on the average to about 1%, with occasional local fluctuations of up to 2% due to scatter in the calibration points. Combining the uncertainty of less than 1 part in 104 in the direct measurement of R with the uncertainty of 1-2% in the measurement of T, a total effective uncertainty in R of just about 1 part in 104 is obtained.

C. Results and Discussion

To within the uncertainty mentioned above the measured resistance of sample W-l was consistent with Equation 6.2 between 1.8-2K and the lowest temperatures reached and the resistance of sample W-3 was consistent with Equation 6.2 between 1.8-2K and 0.15K. shown in Figure 6A where the resistances of sample W-1 (filled circles and right scale) and W-3 (open circles and left scale) are plotted versus T2. The lines drawn are best fits to the data for T < 1.8K. Figure 6B is a more detailed graph of the behavior below 1.0K. In this figure, the resistances R of samples W-1 (filled symbols and right scale) and W-3 (open symbols and left scale) are plotted as functions of T (squares), T² (circles), and T³ (triangles). In each case, the plot of R versus T² yields a straight line over the entire temperature range (except for sample W-3 below 0.1K), while the plots of R versus T and T do not. The lines drawn through the T² plot represent best fit lines to the data for T < 1.8K. The fluctuations about these lines are compatible with the uncertainties discussed above. These lines determine values for the coefficients C in Equation 6.2 of $C = .0075 \times 10^{-8} \Omega/K^2$ for sample W-1 and $C = .0100 \times 10^{-8}$ Ω/K^2 for sample W-3. Using conversion factors (area/ length) of 0.0064 and 0.0065 cm for samples W-1 and W-3 respectively, the coefficients of the T² term in the

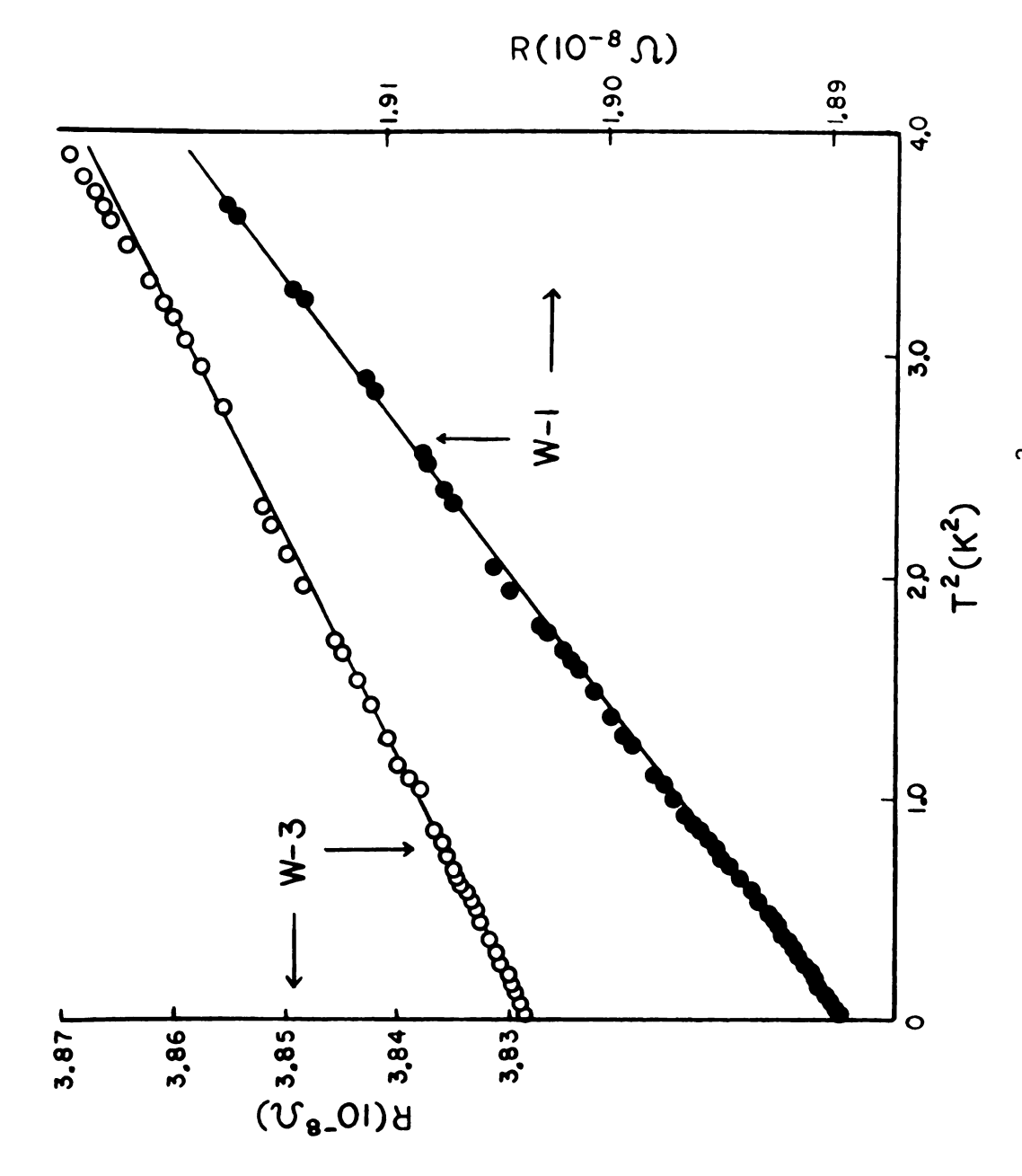
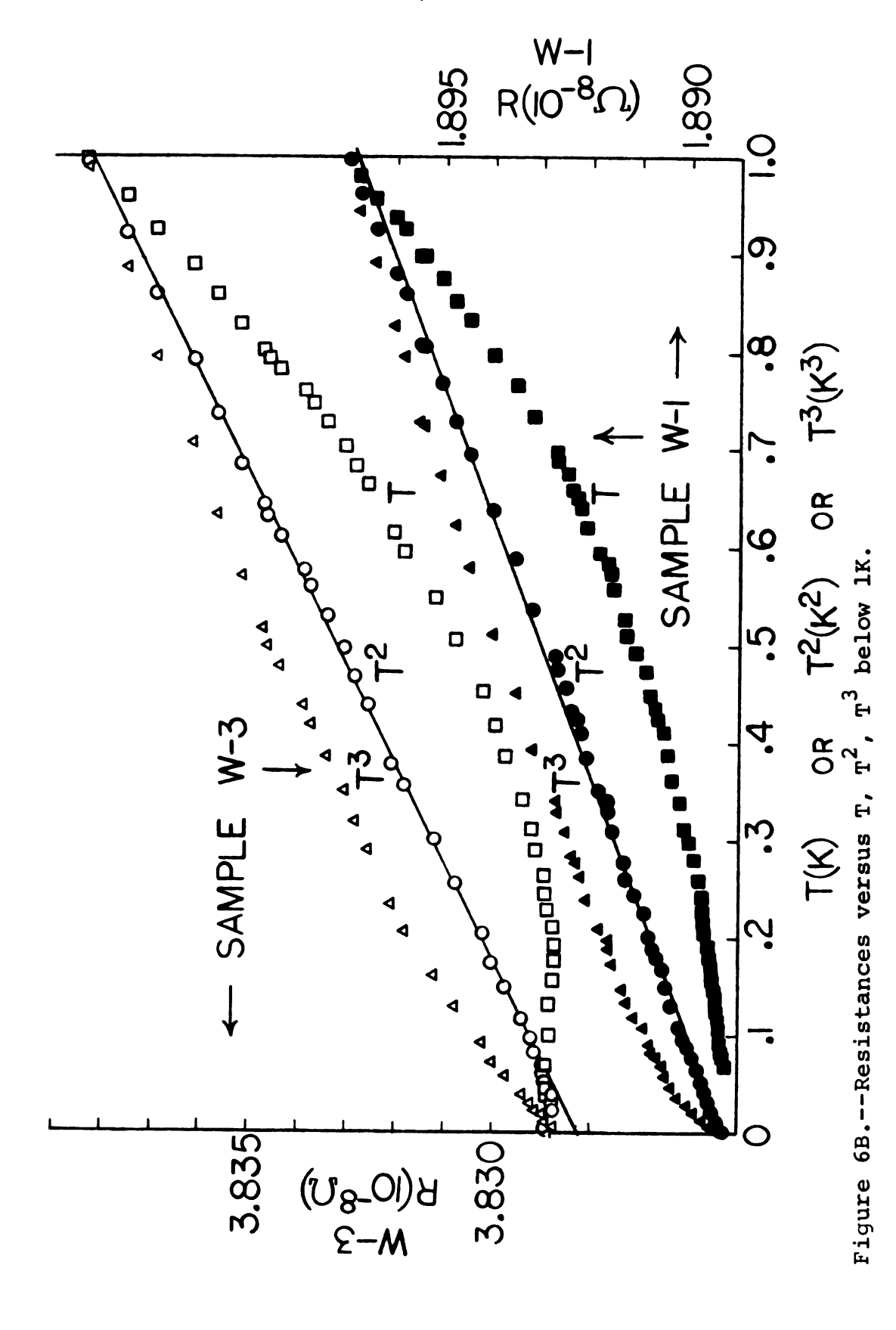


Figure 6A.--Resistances of tungsten samples versus \mathbf{T}^2 below 2°K.



electrical resistivities are found and given in Table 6A. These values are lower than those obtained by previous workers using higher temperature data (T > 1.4K). Since their RRRs span those for our samples, their higher values for A are unlikely to result from Deviations from Matthiessen's rule in less pure samples. Rather, it is more probable that they are errors arising from the use of Equation 6.1 under conditions where all three parameters, $\rho_{\rm O}$, A, and B, had to be determined by a single fit to uncertain data.

Below about 0.15K, the resistance of the "less pure" sample W-3 (RRR = 22,000) rises slightly as the temperature decreases, yielding a resistance minimum such as is usually associated with the presence of a magnetic impurity. This sample also displayed anomalous thermoelectric behavior below about 0.5K (55). Both this resistance minimum and the thermoelectric anomaly suggest that sample W-3 is unlikely to represent "pure tungsten" below 0.15K.

The very low temperature behavior of the "purer sample," W-1 (RRR = 44,000) is now examined. This sample did not evidence either a resistance minimum or an ultralow temperature thermoelectric anomaly. Figure 6B clearly establishes a T² variation for the resistance of sample W-1 down to at least 0.3K. However, below 0.3K the uncertainties in the data become such a large fraction of

TABLE 6A. -- Values for the Coefficient A.

Investigator(s) Sample	Sample RRR	$A(10^{-13}\Omega-cm/K^2)$	
Present Study			
W-1 W-3	44,000 22,000	4.8* 6.4	
Berthel (54)			
Avg.	15,000-330,000	8	
Wagner, Garland and Bowers (44)			
W-7 W-8 W-6 W-2 W-3	95,000 75,000 63,000 59,000 43,000	8.7 11.0 6.7 6.8 7.2	

^{*}The value given for sample W-l supersedes a preliminary value given elsewhere (53). This preliminary value was incorrect due to a systematic error resulting from a small temperature variation of the standard resistance, an error which has now been corrected.

the temperature dependent portion of R that a deviation from T² behavior can no longer be completely ruled out. Examination of this figure shows that if there is such a deviation, it is almost surely toward a slower rather than a faster decrease with decreasing temperature. But this is the opposite of what would be expected if electron-phonon Umklapp scattering were dominant. Therefore it is concluded that the results favor electron-electron scattering as the source of the temperature dependent portion of the very low temperature resistance of tungsten.

CHAPTER VII

THERMOELECTRIC RATIO MEASUREMENTS IN TUNGSTEN AT ULTRA-LOW TEMPERATURES

A. Introduction

In metals, the one dimensional transport equations describing the flow of electric current (J = current density) and of heat current (U = heat current density) under the influence of an electric field E and temperature gradient VT are of the form (56):

$$J = e^{2}K_{O}E + \frac{e}{T}K_{I} (-\nabla T)$$
 7.1

$$U = eK_1E + \frac{1}{T}K_2 (-\nabla T)$$
 7.2

The transport behavior of a given sample can be completely described in terms of the three transport coefficients K_0 , K_1 , and K_2 . Because K_1 is not experimentally directly accessible, measurements of it are usually made in combination with other coefficients. In particular, the thermopower S, which is appropriate for J=0, is defined as,

$$S = \frac{E}{VT} \mid_{J=O} = \frac{1}{eT} \frac{K_1}{K_O}$$
 7.3

Recently, Garland (57) showed that at low temperatures a substantial improvement in precision can usually be obtained if instead of measuring S one measures the thermoelectric ratio G which is defined by

$$G = \frac{J}{U} \mid_{E=O} = \frac{eK_1}{K_2}$$
 7.4

This is functionally similar to S, but appropriate to E = 0 rather than J = 0. Garland showed that G is related to S through the Wiedermann-Franz ratio L,

$$G = \frac{S}{LT}$$
 7.5

Experimentally, G can usually be measured much more precisely than S because one need not measure the temperature gradient VT along the specimen. Garland and VanHarlingen (48) have recently discussed in detail what G is, how it is measured, and why it can often be determined more accurately than S.

At ultra-low temperatures, the dominant scatters of the electrons in a metal will be either impurities or the sample surface. Both types of scatters are normally assumed to scatter electrons elastically. For such a case, L should approach the Lorentz number L_0 , S should decrease linearly with T (58, 59), and thus G would be expected to approach a constant value G_0 as T + 0 K.

Recently, Garland and VanHarlingen (48) measured G for tungsten between 1.2 and 7.0°K. Instead of finding that $G + G_O$ as T decreased, they found that their data fit an equation of the form

$$G(T) = AT^{-\frac{1}{2}} + BT$$
 7.6

for T between 1.3 and 4°K. They were unable to associate either term with a particular scattering mechanism.

These unexpected results provided the stimulation for additional measurements of G in tungsten. The present study was designed to confirm the form found by Garland and VanHarlingen and to extend the measurements to lower temperatures where the $T^{-\frac{1}{2}}$ term should be more important.

B. Present Study

In the present study, thermoelectric ratio G measurements on three high purity single crystal tungsten samples were made at temperatures from 7°K down to below 50 mK. The three specimens were the same tungsten rods used in the electrical resistivity measurements described in Chapter VI. The ${\rm He}^3$ - ${\rm He}^4$ dilution refrigeration system was also the same. Figure 7A shows the variation with temperature of G for the "purest" sample, sample W-1, a three-pass zone-refined single crystal having 1.4 mm diameter and a Residual Resistance Ratio (RRR = $R_{300°K}/R_{0°K}$) of 44,000. As expected from the simple theory,

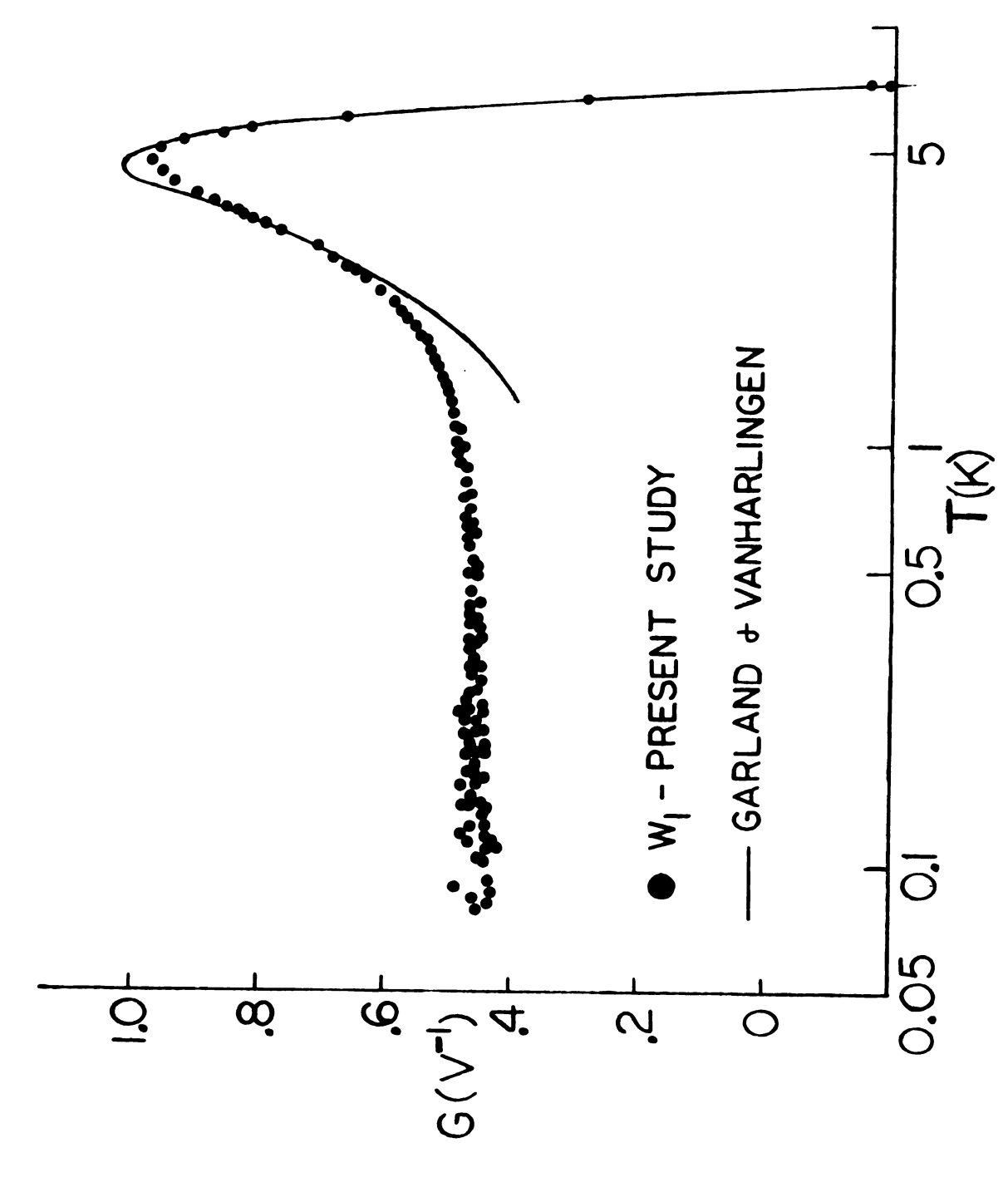


Figure 7A.--Thermoelectric ratio of tungsten.

but in contradiction to Equation 7.6, below about 0.5°K G is constant to within experimental uncertainty down to 0.07°K, the lowest temperature studied with this sample.

The data shown in Figure 7A were obtained during three different measuring runs, the first and last occurring three months apart. For comparison, the solid curve in Figure 7A indicates the behavior of G for a sample with RRR = 60,000 as reported by Garland and VanHarlingen (48). The similarity between this curve and the data of the present study in the region of overlap provides support for the basic validity of both sets of measurements. In view of its agreement with the simple form expected, the low temperature behavior of sample W-1 is probably representative of high purity tungsten in which the scattering of electrons is dominated below 1K by impurities for which simple potential scattering applies.

In contrast to both the simple form of G for sample W-1 and Equation 7.6, quite a different behavior was observed in two 1.4 mm diameter "less pure" samples: W-2, a two-pass zone-refined single crystal having RRR = 34,000; and W-3, a one-pass zone-refined single crystal having RRR = 22,000. In Figure 7B G for samples W-2 and W-3 (solid curves) is compared with G for sample W-1 (dashed line) at temperatures below 1K. Whereas for sample W-1, G is constant below 1K; for samples W-2 and

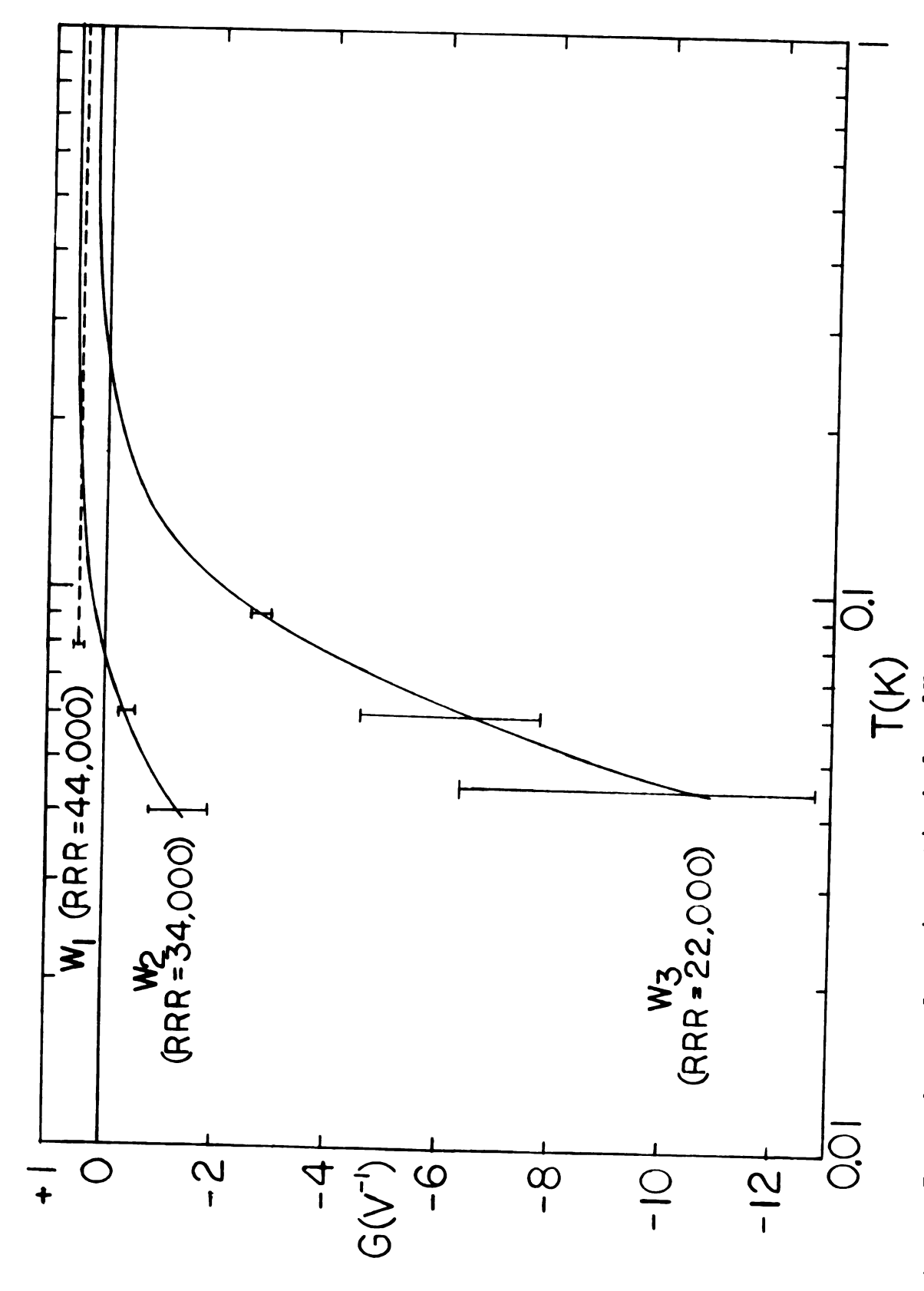


Figure 7B. -- Thermoelectric ratio below 1K.

W-3, G became increasingly more negative with decreasing temperature to the lowest temperatures reached. This is opposite of the behavior evidenced by the samples of Garland and VanHarlingen where G became more positive for the less pure samples as the temperature decreased. At the lowest temperatures reached in the present study, the accuracy of the data was limited by the fact that the measured thermal voltages were comparable to the Johnson noise in the system (approximately 10⁻¹⁵ volts).

According to the third law of thermodynamics, the thermopower of a sample must approach zero as T + 0°K. To investigate whether this is occurring in the ultra-low temperature range, one can multiply G by L T to form a "pseudo-thermopower." Figure 7C shows $\operatorname{GL}_{\mathcal{O}}$ T for the three samples at temperatures below 0.3K. For sample W-1, $\operatorname{GL}_{\mathcal{O}}^{\mathbf{T}}$ is positive at 0.3K and decreases toward zero linearly with decreasing temperature. For samples W-2 and W-3 , on the other hand, $GL_{O}T$ is initially positive, but then passes through zero and becomes increasingly negative with decreasing temperature. At 45mK the magnitude of $\operatorname{GL}_{\mathcal{O}}^{\mathsf{T}}$ for sample W-3 is about 20 times larger than that for sample W-1. Because of the third law, GLOT cannot continue to become more negative indefinitely as T decreases. At some temperature it must reach a peak negative value and then begin to decrease in magnitude back toward zero. To locate this peak will require still

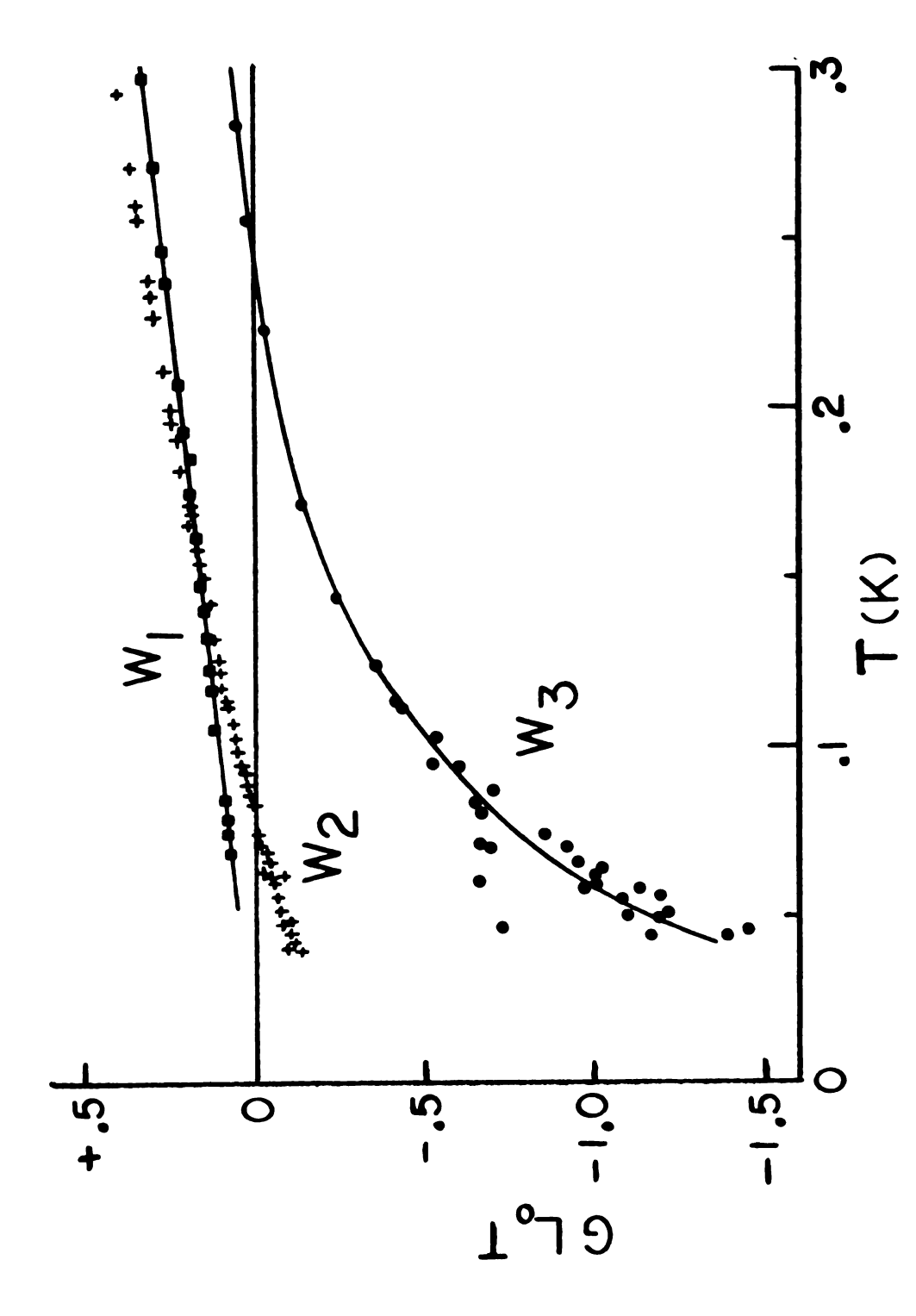


Figure 7C.--Pseudo-thermopower below 0.3K.

lower temperatures than presently reached, perhaps even temperatures lower than the superconducting transition temperature of tungsten ($\simeq 12-16 \text{mK}$) (60,61). In such a case, it will be necessary to apply a small magnetic field (H \simeq lg) to suppress the superconducting transition.

Both the negative sign and the large magnitude of the anomaly in GL_OT for samples W-2 and W-3 are reminiscent of the behavior of the thermoelectric anomalies produced by dissolved impurities whose magnetic properties are important (59, 62). Such anomalies are usually accompanies by the appearance of a resistance minimum (62). Indeed, upon investigation, a very small resistance minimum for sample W-3 was discovered--a fractional increase in resistivity of about 1 part in 10⁴ between 0.2K and 50mK (63). No minimum was found for samples W-1 or W-2.

To follow up this evidence, all three samples were analyzed by spark source mass spectrometry. As is shown in Table 7A, a search for over 50 elements revealed only three with apparent concentrations greater than 100 atomic ppm: C, Si, and Fe. Of these three, the only one known to produce magnetically related anomalies is Fe, which has been found to produce giant thermopowers and resistance minima in a number of metals (59, 62, 64). In tungsten, evidence of magnetic properties of Fe has been obtained

TABLE 7A. -- Reported Impurity Concentrations.

Impurity	W-1			*** 0	
	A	В	С	W-2	W-3
С	3000	10000	3500	6000	13000
Si	280	640	410	510	700
Fe	80	330	350	170	300
Cr	40	110	340	60	95
Pt	90	70	40	35	75
Au	15	40	35	25	60
Ni	7	35	30	20	30
Ti	ND	35		30	20
Al	<7	30	25	25	25
Mg	<30	15	15	15	20

A, B, and C are independent tests on the same sample W-1. 40 other elements were tested for, but not detected or were less than 1 ppm or had interferences associated with them. Reported by Analytical Laboratory, Material Science Center, Cornell University, Ithaca, N.Y.

from measurements of magnetic susceptibility (65) and from Mössbauer measurements (66).

From all this information, it is inferred that

Fe is the most likely candidate for the source of the

observed anomalous behavior. However, neither the

reported concentrations of Fe, nor those of any of the

other impurities detected, correlate with the magnitudes

of the thermoelectric anomalies. This lack of correlation may result from different properties of Fe ions in

different states. There is evidence for host metals such as Cu, that Fe ions in solution produce anomalous thermoelectric behavior, whereas Fe ions bound in oxides do not (67). If this is also true in tungsten, then the total concentration of Fe would not necessarily correlate with the magnitude of the thermoelectric anomaly.

In conclusion, the following points should be The present study did not confirm the form for G proposed by Garland and VanHarlingen. Instead for tungsten samples of sufficient purity, the form for G at temperatures below 0.5K is a constant as expected from simple theory. For less pure tungsten samples, a new ultra-low temperature anomaly has been observed which may be plausibly attributed to Fe ions in very dilute solution. However, a definitive determination of the source of this anomaly will require further studies including: ultra-low temperature transport measurements on carefully prepared and well characterized W(Fe) alloys; magnetic susceptibility measurements to search for direct evidence of magnetic behavior; and studies of effects of oxidation on the magnetic behavior and the thermoelectric properties of the allowy.

LIST OF REFERENCES

LIST OF REFERENCES

- 1. Khoshnevisan, M., Ph.D. Thesis, Michigan State University (1973).
- Müller, E. W., Z. Physik 131, 136 (1951).
- 3. Müller, E. W., J. Appl. Phys. 27, 474 (1956).
- 4. Müller, E. W., Phys. Rev. 102, 624 (1956).
- 5. Müller, E. W., Bull., Am. Phys. Soc. 7, 27 (1962).
- 6. Ralph, B., and Brandon, D. G., Phil. Mag. <u>8</u>, 919 (1963).
- 7. Southworth, H. N., and Ralph, B., Phil. Mag. 14, 383 (1966).
- 8. Tsong, T. T., and Müller, E. W., Appl. Phys. Lett. 9, 7 (1966).
- 9. Tsong, T. T., and Müller, E. W., J. Appl. Phys. 38, 545 (1967).
- 10. Tsong, T. T., and Müller, E. W., J. Appl. Phys. 38, 3531 (1967).
- 11. DuBroff, W., Ph.D. Thesis, Columbia University (1967).
- 12. DuBroff, W., and Machlin, E. S., Phil. Mag. <u>18</u>, 453 (1968).
- 13. Chen, C. G., Ph.D. Thesis, Cornell University (1974).
- 14. Speicher, C. A., Pimbley, W. T., Attardo, M. J., Galligan, J. M., and Brenner, S. S., Phys. Lett. 23, 194 (1966).
- 15. Berger, A. S., Seidman, D. N., and Balluffi, R. W., Acta Met. 21, 123 (1973).
- 16. Chen, C. G., and Balluffi, R. W., Acta Met. 23, 919 (1975).

- 17. Khoshnevisan, M., and Stephan, C. H., J. Phys. E: Sci. Inst. 6, 1025 (1973).
- 18. Schwerdtfeger, K., and Muan, A., Acta Met. 12, 905 (1964).
- 19. Rudman, P. S., and Averbach, B. L., Acta Met. <u>5</u>, 65 (1957).
- 20. Tissier, T. T., and Tournier, R., Sol. State Comm. 11, 895 (1972).
- 21. Swallow, G. A., Williams, G., and Grassie, A. D. C., Phys. Rev. B 11, 337 (1975).
- 22. Swallow, G. A., and White, R. J., Phys. Lett. 44A, 521 (1973).
- 23. Temperature, Its Measurement and Control in Science and Industry, Reinhold Publ. Co., New York (1941) p. 1318.
- 24. Hansen, M., Constitution of Binary Alloys, McGraw-Hill Book Co., New York (1958) p. 492.
- 25. Kucera, J. and Zemcik, T., Can. Met. Quart. <u>7</u>, No. 2, 83 (1968).
- 26. Müller, E. W., and Tsong, T. T., Field Ion Microscopy; Principles and Applications, American Elsevier Publ. Co., New York (1969) p. 120.
- 27. Schwerdtfeger, K., and Muan, A., Acta Met. <u>13</u>, 509 (1965).
- 28. Brändi, G., and Olsen, J. L., Mater. Sci. Engng. 4, 61 (1969).
- 29. Larson, D. C., Physics of Thin Films 6, 81, Academic Press, New York (1971).
- 30. Baer, D. R., and Wagner, D. K., J. Low Temp. Physics <u>13</u>, 445 (1973).
- 31. Dausinger, F., Der Dickeneffekt der elektrschen Leifähigkeit an Wolfram, Diplomarbeit, Institut für Theoretische und Angewandte Physik der Universität Stuttgart und Max-Planck-Institut für Metallforschung, Institut für Physik (1973), (Unpublished).

- 32. Startsev, V. Ye., Volkensteyn, N. V., and Nikitina, G. A., Fiz. Metalloved 26, 261 (1968), (Engl. Transl. 26, No. 2, 76).
- 33. Olsen, J. L., Proc. Intern. Conf. Elec. and Magnetic Peoperties of Thin Metallic Layers, Louvain, 1961. Vlaamse Academie voor Wetenschappen (1961), p. 338.
- 34. Sparlin, D. M., and Marcus, J. A., Phys. Rev. <u>144</u>, 494 (1966).
- 35. Girvan, R. F., Gold, A. B., and Phillips, R. A., J. Phys. Chem. Solids 29, 1485 (1968).
- 36. Meaden, G. T., Electrical Resistance of Metals, Plenum Press, New York (1965).
- 37. Park, J. Y., Huang, W. C., Berger, A. S., and Balluffi, R. W., Defects and Defect Clusters in B.C.C. Metals and Their Alloys, p. 420 (National Bureau of Standards, Gaithersburg, Maryland, 1973).
- 38. White, G. K., and Tainsh, R. J., Phys. Rev. Lett. 19, 165 (1967).
- 39. Schriempf, J. T., J. Phys. Chem. Solids <u>28</u>, 2581 (1967).
- 40. Schriempf, J. T., Phys. Rev. Lett. 20, 1034 (1968).
- 41. Schriempf, J. T., Sol. State Comm. 6, 873 (1968).
- 42. Anderson, A. C., Peterson, R. E., and Robischaux, J. E., Phys. Rev. Lett. 20, 459 (1968).
- 43. Beitchman, J. G., Trussel, C. W., and Coleman, R. V., Phys. Rev. Lett. 25, 1291 (1970).
- 44. Wagner, D. K., Garland, J. C., and Bowers, R., Phys. Rev. <u>3B</u>, 3141 (1971).
- 45. Ziman, J. M., Electrons and Phonons, Claredon Press, London (1960) p. 415.
- 46. Mott, N. F., Advan. Phys. 13, 325 (1964).
- 47. Compilation by Phillips, N., and Pearlman, N., quoted in Kittel, C., Introduction to Solid State Physics (4th Ed.), John Wiley and Sons, New York (1971) Table 2, p. 254.

- 48. Garland, J. C., and VanHarlingen, D. J., Phys. Rev. 10B, 4825 (1974).
- 49. Wagner, D. K., Phys. Rev. B5, 336 (1972).
- 50. Lawrence, W. E., and Wilkins, J. W., Phys. Rev. <u>B6</u>, 4466 (1972).
- 51. Schotte, D., and Schotte, U., Sol. State Comm. <u>10</u>, 131 (1972).
- 52. Imes, J., Ph.D. Thesis, Michigan State University (1974).
- 53. Stone, E. L. III, Ewbank, M. D., Bass, J., and Pratt, W. P. Jr., Bull. Am. Phys. Soc. 21, 389 (1976).
- 54. Berthel, K. H., Phys. Stat. Sol. 5, 399 (1964).
- 55. Stone, E. L. III, Ewbank, M. D., Pratt, W. P. Jr., and Bass, J. (to be published).
- 56. Ziman, J. M., Principles of the Theory of Solids, University Press, London (1972) p. 230.
- 57. Garland, J. C., Appl. Phys. Lett. 22, 203 (1973).
- 58. Blatt, F. J., Physics of Electronic Conduction in Solids, McGraw-Hill Inc., New York (1968).
- 59. Barnard, R. D., Thermoelectricity in Metals and Alloys, Taylor and Francis Ltd., London (1972).
- Black, W. C., Johnson, R. T., and Wheatley, J. C.,
 J. Low Temp. Phys. <u>1</u>, 641 (1969).
- 61. Triplett, B. B., Phillips, N. E., Thorp, T. L., Shirley, D. A., and Brewer, W. B., J. Low Temp. Phys. 12, 519 (1973).
- 62. MacDonald, D. K. C., Thermoelectricity: An Introduction to the Principles, John Wiley and Sons,
 New York (1962).
- 63. Stone, E. L. III, Ewbank, M. D., Bass, J., and Pratt, W. P. Jr. (submitted for publication).
- 64. Heeger, A. J., Solid State Physics, 23, 284 (1969).

- 65. Thomas, L. K., and Sellmyer, D. J., 18th Annual Conference on Magnetism and Magnetic Materials, Denver, Colorado (November, 1972).
- 66. Kitchens, T. A., Steyert, W. A., and Taylor, R. D., Phys. Rev. 138, A467 (1965).
- 67. Gold, A. V., MacDonald, D. K. C., Pearson, W. B., and Templeton, I. M., Phil. Mag. 5, 765 (1960).
- 68. Reference 26, p. 41.
- 69. Oppenheimer, J. R., Phys. Rev. 31, 67 (1928).
- 70. Messiah, A., Quantum Mechanics, Interscience Publishers, New York (1962).
- 71. Reference 26, p. 44.
- 72. Müller, E. W., J. Appl. Phys. 28, 1 (1957).
- 73. Mulson, J. F., and Müller, E. W., J. Chem. Phys. 38, 2615 (1963).

APPENDICES

<u></u>	 7		

APPENDIX A

DETAILS OF COMPUTER ANALYSIS

APPENDIX A

DETAILS OF COMPUTER ANALYSIS

This appendix contains a more detailed account of the procedure involved in determining the shift between layers and the transformations involved in determining the relative positions of atoms on successive layers. In Chapter II, the scanning of the film and the recording of the frame numbers giving the locations of the signatures on the film was described. Certain planes have more regular grid networks or better resolution. are chosen for the more detailed analysis involved in the determination of the radial distribution function. first step of the analysis is to digitize the atomic positions. Next the data are fed into the main computer program and sorted. The data points for layer origins and Co sites are handled separately, yet use some of the same transformations and subroutines. When the relative positions of all the Co atoms have been determined, a subroutine calculates the radial distribution function. The specifics of this procedure are described below.

A. Digitizing and Sorting

As mentioned in Chapter II, the atomic sites were digitized using the High Energy Physics scanning tables. The x and y coordinates of any site on the film could be displayed and then recorded on magnetic tape. There also existed two sets of thumbwheels which allowed additional information to be recorded. The information was encoded on the magnetic tape in the form of data records, which consist of a number of data points (atomic positions) plus the settings of the two thumbwheels and a function There were three basic types of data records: layer origin, Co sites, and atomic positions of all atoms on the layer. This set of three was taken for each layer from a frame of film which showed all the central atoms of that layer clearly. The different types of data records and how to sort them according to their function code is described in detail below.

The relative positions of two atoms on different layers cannot be measured directly since only one layer at a time can be imaged. It was therefore necessary to specify their positions relative to a third point which itself was fixed with respect to the FIM tip. It was found that the image of the tip and the image from the data box on the film remained constant. Therefore, a dot on the watch in the data box was used as the fixed reference point. The relative positions of any two atoms

with respect to this watch origin could be measured by the scanner, and by subtracting one from the other, the vector connecting them could be known in terms of the scanner (X,Y) coordinate system.

1. Layer Origin Data Record

This data record contained the watch origin, the position of the arbitrary origin 0 of a given layer, and the positions of atoms A and B as given in Figure 4B.

The vectors \overline{OA} and \overline{OB} specified the planar coordinate system. \overline{OA} was always chosen to point toward the local {101} plane and the vector \overline{OB} to point toward the local {111} plane. The location of any atom on the planar layer could then be specified with respect to the origin in terms of the planar coordinates (M,N).

2. Co Site Data Record

This data record contained the positions of the layer origin and of the vacant site. The planar coordinates (M,N) were also set on the thumbwheels to provide a double check.

3. All Atom Data Record

This data record contained the watch origin and all the atomic sites of the planar layer. These data records were used in the plotter program where the atomic sites of successive layers were plotted and the shift between layers checked by eye.

The first task of the main computer program was to read in the data records off the magnetic tape, decode them and sort them according to their function code. The flow chart for this is shown in Figure AA.

B. Transforming Scanner Coordinates to Planar Coordinates

The transformation for a given atom D from (X,Y) scanner coordinates to (DA,DB) planar coordinates is done using the layer origin data record. The layer origin O plus atom sites A and B serve to specify unit vectors \overline{OA} and \overline{OB} . As shown in Figure 4B, \overline{OA} and \overline{OB} in terms of planar coordinates are written (1,0) and (0,1), respectively. In terms of the (X,Y) scanner coordinate system OA and OB have components (AX,AY) and (BX,BY), respectively. An arbitrary point, for example site D, which is specified by the vector OD and scanner coordinates (DX,DY) can be transformed into planar coordinates (DA,DB). The standard matrix transformation is as follows:

$$\begin{pmatrix} DA \\ DB \end{pmatrix} = \frac{1}{(AX)(BY) - (AY)(BX)} \begin{pmatrix} BY & -BX \\ -AY & AX \end{pmatrix} \begin{pmatrix} DX \\ DY \end{pmatrix}$$

Using this transformation, the position of atom D, which could be the location of α -dark spot on the top layer, is transformed into planar coordinates (-1,2). This transformation is also used to help find the shift from origin O to the origin of the first layer below, atom O'. The

details of the shift of origins from layer to layer is covered below in section D.

C. Transforming Planar Coordinates to FCC Cartesian Coordinates

The transformation of (DA,DB) planar coordinates to FCC coordinates was covered in Chapter IV for the specific case of one layer of the {315} plane. In general, the transformation can be used to transform any point, either atom D, O', or C, where the planar coordinates are known, into local FCC coordinates both relative to the origin at atom O. The FCC cartesian coordinates system is specified by the unit axis vectors of the lattice, (100), (010), and (001).

The general case for a site D with planar coordinates (M,N) on the same layer is as follows.

$$DX = XO + (M)(S(3,J)) + (N)(S(6,J))$$

$$DY = YO + (M)(S(4,J)) + (N)(S(7,J))$$

$$DZ = ZO + (M)(S(5,J)) + (N)(S(8,J))$$

where the origin in FCC is (XO,YO,ZO). J specifies the type of plane, i.e., whether {315} or {213}. The particular values of S(I,J) are given in Table AA. The general case for a transformation of site O' relative to origin O is handled below.

TABLE AA. -- The Transformation Parameters.

	{315}	{213}
S(1,J)	0.45	-0.50
S(2,J)	0.25	0.25
S(3,J)	1.0	1.0
S(4,J)	-0.5	-0.5
S(5,J)	-0.5	-0.5
S(6,J)	0.5	0.0
S(7,J)	1.0	1.5
S(8,J)	-0.5	-0.5
S(9,J)	0.5	-0.5
S(10,J)	0.0	0.5
S(11,J)	-0.5	0.0

D. Shift of Origins for Successive Layers

The procedure to find the relative coordinates of two origins on successive layers in the common FCC coordinate system is only slightly more involved than the preceding transformations. Since the two layers cannot be imaged simultaneously, the use of the watch origin as a fixed reference point is essential. If the origins of two successive layers are O and O', the connecting vector \overline{OO} ' is originally specified in terms of the scanner coordinate system (see Figure 4B). Using the vectors \overline{OA} and \overline{OB} and the transformation already laid down, \overline{OO} ' can be expressed in terms of the planar coordinate system.

As can be seen from the schematic diagram (Figure 4B) or the ball model (Figure 4A), the vector $\overline{00}$ ' will not be a linear combination of integral multiples of vectors OA and \overline{OB} . This is due to the shift in the projection of the crystallographic plane between layers one and two. The shortest vector between the layers is \overline{OC} , which is a shift between first nearest neighbors. This vector OC can be specified in terms of \overline{OA} and \overline{OB} , and also in terms of the FCC coordinates. In particular, for the {315} plane, the shift in FCC coordinates is: OC = (0.5, 0.0,-0.5). In general the shifts are given by S(9.J), S(10.J) and S(11.J) of Table AA. This known shift \overline{OC} can be subtracted from $\overline{00}$ ' leaving vector $\overline{00}$ ' in the second laver. In the ideal case CO' is a linear combination of integral multiples of OA and ON. For example, in Figure 4B, CO' can be written (1,-1) in terms of the planar coordinate system. The transformation of CO', a general vector in one layer with planar coordinates (M,N), to FCC coordinates was given earlier in section C.

The total layer shift of origins \overline{OO} ' can now be straightforwardly transformed into FCC coordinates. In general this transformation is:

$$XO' = XO + S(9,J) + (M)(S(3,J)) + (N)(S(6,J))$$

$$YO' = YO + S(10,J) + (M)(S(4,J)) + (N)(S(7,J))$$

$$ZO' = ZO + S(11,J) + (M)(S(5,J)) + (N)(S(8,J))$$

The atoms on the second layer can then be expressed in FCC coordinates relative to their local origin (XO', YO', ZO'). The relative coordinates of all atoms in terms of the common FCC coordinate system are then known.

E. Radial Distribution Function Calculation

The essential part of the radial distribution function calculation is the counting of the number of ith nearest neighbor pairs. The distance between ith nearest neighbors in terms of the FCC lattice parameter can be determined with the help of a ball model. The counting of pairs is then simply a matter of taking each pair of Co atoms with their known common coordinates and calculating the distance between them. This number of pairs for each nearest neighbor shell is then normalized using the expression in Chapter IV.

F. The Significance of the Transformation Parameters

In the computer program, the transformation parameters are stored in an array S(I,J). J designates the plane, either {315} or {213}, being analyzed, I designates the transformation or shift that is to be carried out. The significance of the S(I,J) is as follows:

S(1,J), S(2,J): The projection of the shift between layers \overline{OC} in terms of fractions of $|\overline{OA}|$ and $|\overline{OB}|$ of the surface coordinate system. These projections are averages from actual FIM images.

S(3,J), S(4,J), S(5,J): The coordinates of atom A with respect to origin O in the FCC coordinate system.

S(6,J), S(7,J), S(8,J): The coordinates of atom B with respect to origin O in the FCC coordinate system.

S(9,J), S(10,J), S(11,J): The coordinates of atom C with respect to origin O in the FCC coordinate system. Atom C is a first nearest neighbor of atom O.

The values of these transformation parameters for the {315} and {213} planes are given in Table AA.

G. Flow Chart of Computer Programs

The flow chart for the major portion of the computer program is shown in Figure AB. The parts of the program using the same subroutine or basic transformation are marked. The sorting portion of the program is given in Figure AA.

The flow chart for the plotter program is presented in Figure AC. The plotter program plotted out all the atomic sites of several successive layers. These plots could then be examined by eye and checks made on the shift of origins from one layer to the next.

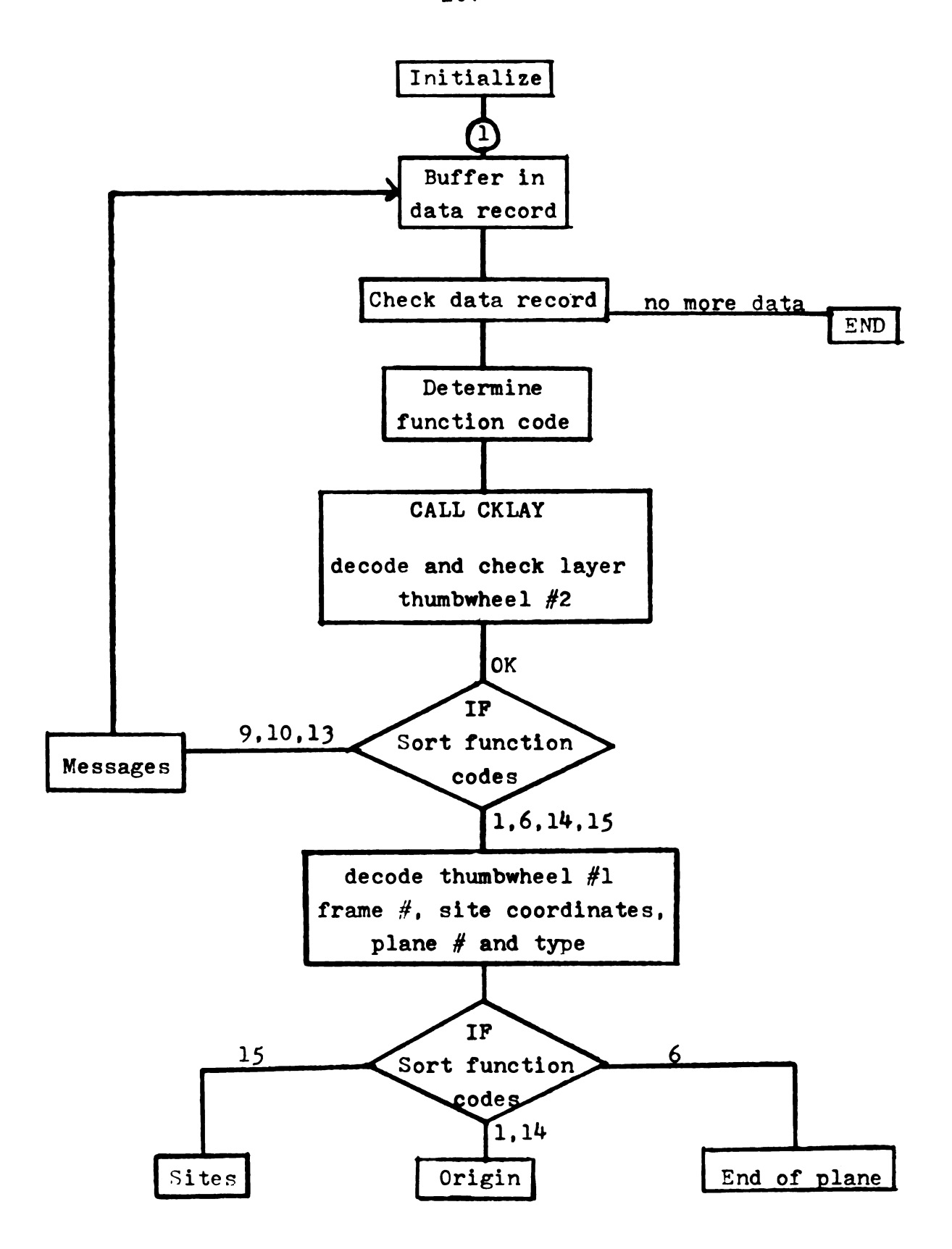


Figure AA. -- Sorting Program.

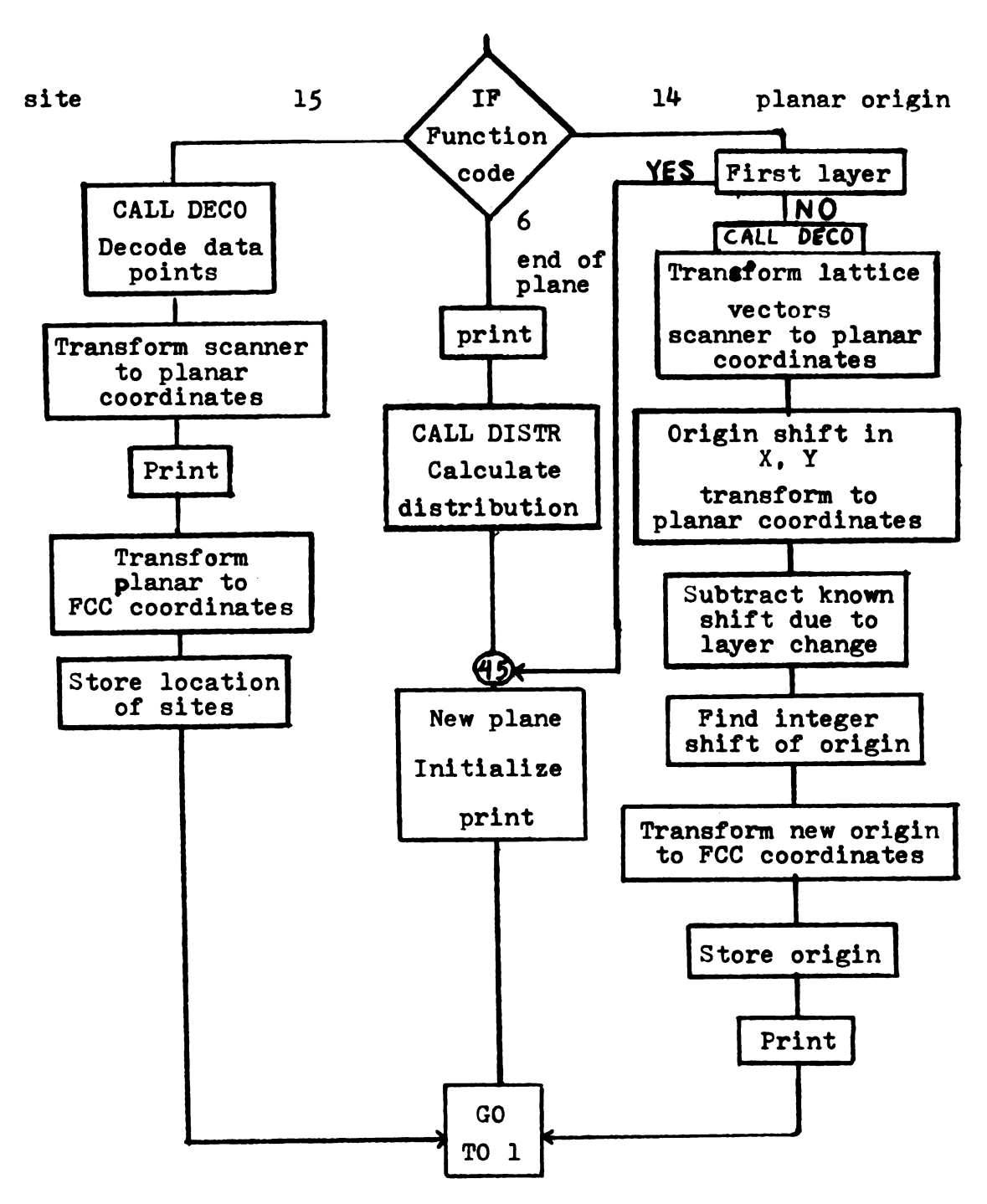


Figure AB.--Body of main program.

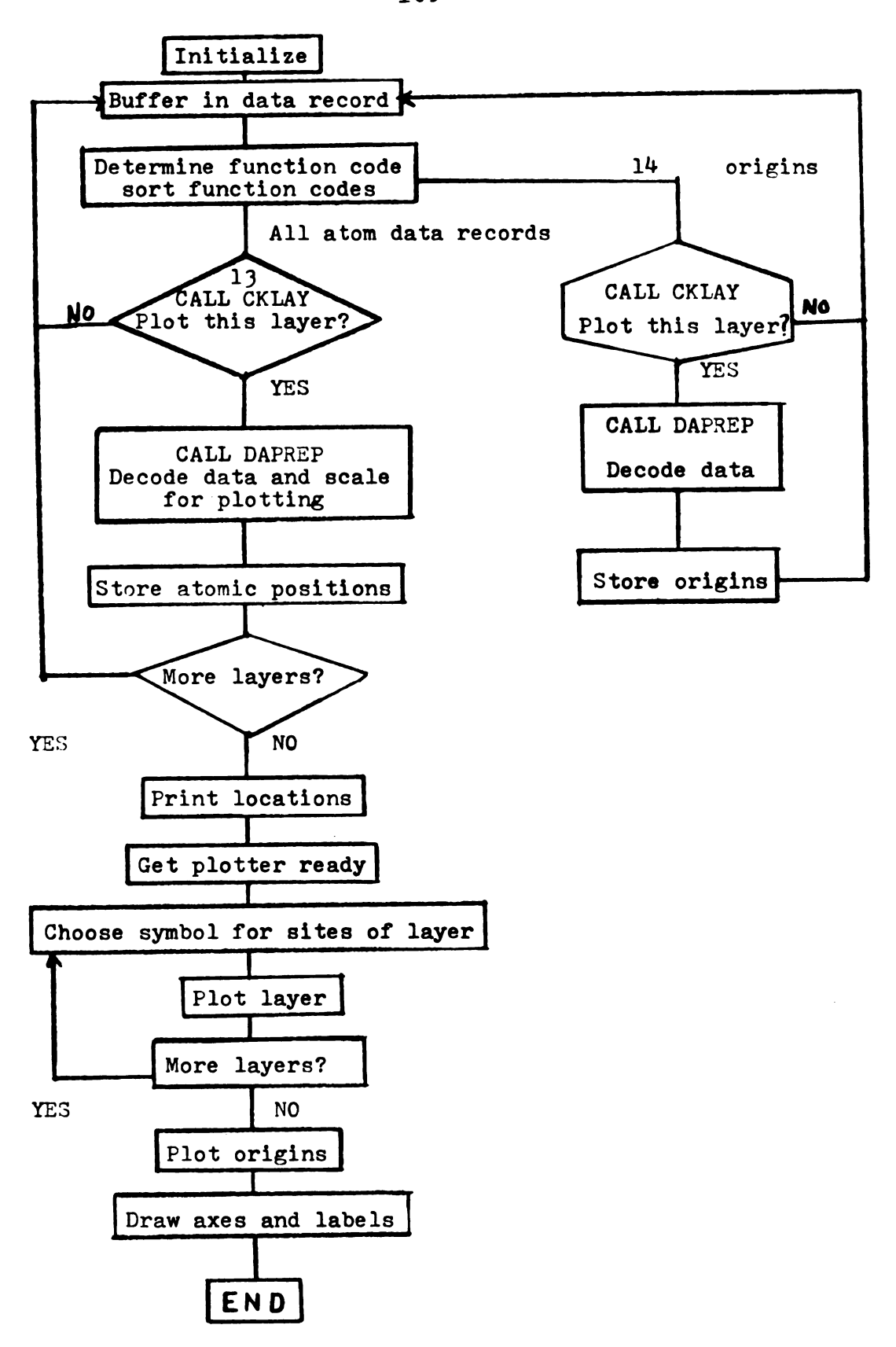


Figure AC. -- Plotter program.

APPENDIX 'B

BASIC PRINCIPLES OF THE FIELD ION MICROSCOPE

APPENDIX B

BASIC PRINCIPLES OF THE FIELD ION MICROSCOPE

To assist the reader in understanding the operation of the field ion microscope, a brief description of the basic apparatus and the principles involved in its operation are given below.

A. The Basic Apparatus

Figure BA illustrates the major features of a simple glass FIM. The fundamental constituents of the microscope are: (1) a specimen in the form of a wire with a very fine hemispherical tip of diameter 100 to 1000Å; (2) a power supply to raise the sample to high electrical potential; (3) an imaging gas (usually He) which will ionize in a sufficiently high electric field, yielding ions which move out along field lines to strike a fluorescent screen; and (4) a fluorescent screen which provides from each region a light output proportional to the number of ions striking that region. As we will describe below, the imaging gas atoms are ionized preferentially at locations directly over atomic sites of the sample tip; the ions then move out radially along field lines and strike the fluorescent screen, producing

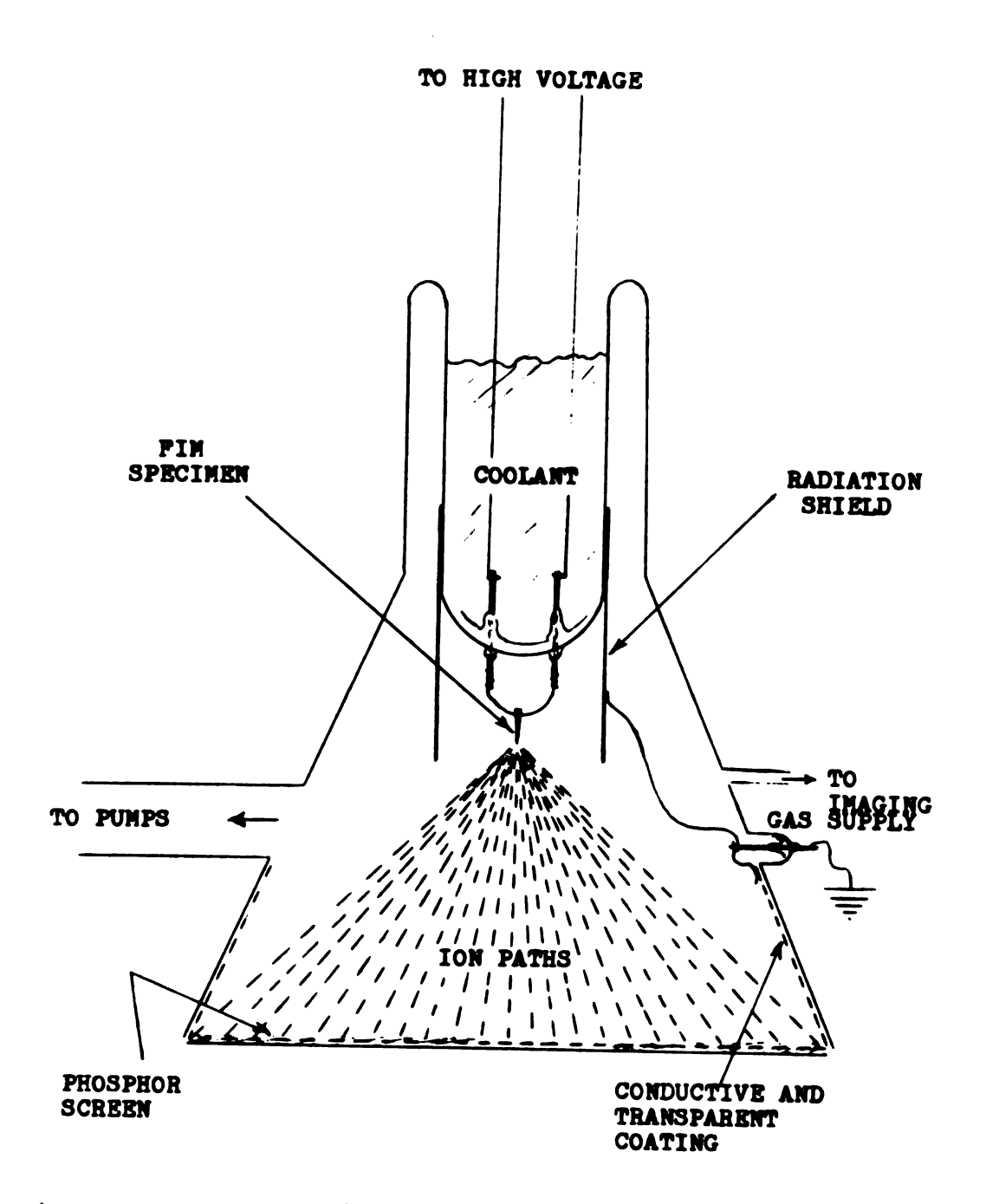


Figure BA.--Schematic diagram of a glass field ion microscope.

thereon a greatly magnified image of the tip. The magnification of the microscope is purely geometric, and is given by

$$M = \frac{R}{\beta r_{+}}$$
 B.1

where R is the distance from the tip to the screen, r_t it the tip radius and β is a geometrical factor (typical values 1.5 to 1.8 (68). For typical values of R = 4cm, r_t = 400A, a magnification of about 6 x 10⁵ or more can be obtained (at the expense of image intensity), but this will not result in any improvement in resolution. As we will discuss below, the resolution of the FIM is independent of R and depends on other variables. It is for optimizing these variables that the major features of the FIM are selected as those shown in Figure BA.

We now describe in more detail the physical principles upon which the microscope operates.

B. Field Ionization

The physical effect responsible for the operation of the microscope is quantum mechanical tunneling, as first envisioned by Oppenheimer (69). When a free neutral atom enters a region of high electric field in space, its outer electron has a non-zero probability of tunneling out and field ionizing the atom in the process. Figure BB(a) shows a simplified one-dimensional potential energy

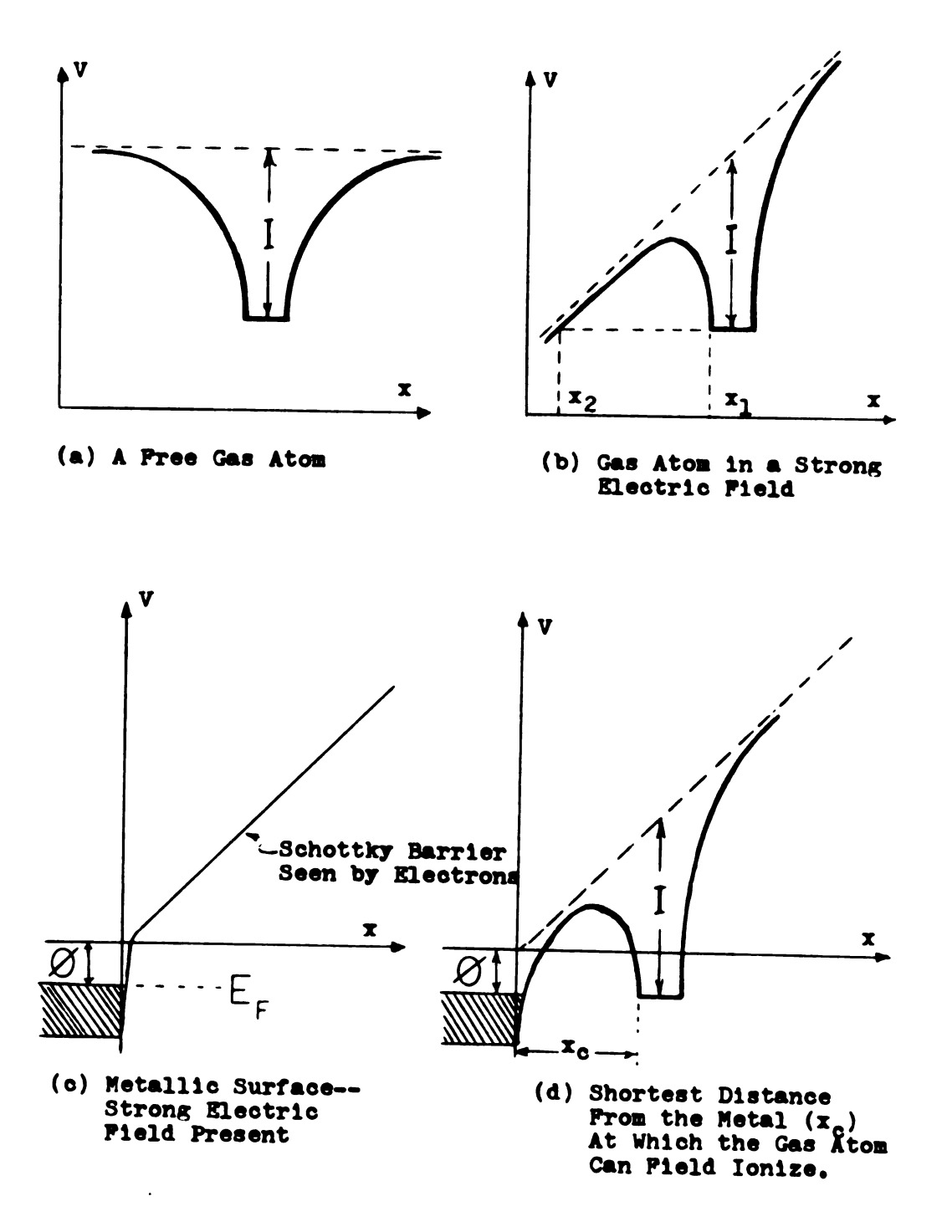


Figure BB.--One dimensional potential energy diagrams for field ionization.

diagram for a ground state outer electron in the potential well of a gas atom with ionization energy I. The distorted potential well of the same atom in a strong electric field is shown in Figure BB(b). The width of the potential barrier (between x_1 and x_2) and its form can be used [by W.K.B. Approximation (70)] to calculate tunneling probabilities for the electron.

The necessary electric field for field ionizing gases in a finite time is of the order of several hundred million volts per centimeter (e.g., 440MV/cm for helium). In 1951 Müller (2) was able to field ionize hydrogen by creating the necessary electric field applying only modest voltages to a sharply pointed tip of a tungsten specimen. At the same time, he discovered that field ionization over the surface of the tip is extremely sensitive to atomic configuration of the surface. Field ionization near a metallic surface is complicated by the effect of the proximity of the conductor on the potential barrier of the electron. Qualitatively, the situation is shown in Figure BB(c) and BB(d).

The Schottky barrier as seen by the conduction electrons at the surface of a metal (with work function \emptyset) after the application of a large positive potential is shown in Figure BB(c). As the imaging gas atom approaches the surface of the metal, the width of the potential barrier for the electron decreases with a resulting

increase in the tunneling probability. When the ground state energy of the electron reaches the top of the Fermi level (E_f) in the metal, the ionization probability is a maximum [Figure BB(d)]. Beyond this critical distance the electron no longer can tunnel into the metal since its energy level sinks below the fully occupied Fermi sea of the metal. The ionization probability abruptly falls to zero, the electron is repelled from the surface, and the atom rebounds.

A rough calculation for helium as imaging gas over a tungsten tip yields a value of $x_C^{~~\approx~}$ 4Å for this critical distance.

C. Resolution of the FIM

A conventional field ion microscope operating at temperatures lower than 25K and with helium as imaging gas has a resolution which is often between 2 to 3Å, smaller than atomic separation on many crystallographic planes of metals. At present no completely rigorous theory for the calculation of the resolution exists, but a simplified model (71) yields the following result which serves as a very useful guide for estimating the resolution of the microscope.

$$\delta = \delta_{o} + \left[4\left(\frac{\beta^{2}r_{t}^{2} \pi^{2}}{2eMV_{o}}\right)^{\frac{1}{2}} + 16\left(\frac{\beta^{2}r_{t}^{2}kT}{eV_{o}}\right)\right]$$
 B.2

Here δ is the resolution and $\delta_{_{\mbox{\scriptsize O}}}$ is due to the effect of the size of the imaging gas atom and is assumed to be of the order of the atomic radius of the imaging The variables given in the above formula are the best image voltage V_0 , the tip radiue r_+ , the mass of the imaging gas atom M, and the effective temperature of the gas T. Electron change (e), Boltzmann constant (k) and Planck's constant divided by $2\pi(\bar{h})$ are known constants. The first term in the brackets is due to the increased uncertainty in the tangential momentum of the gas atom as it becomes localized (Heizenberg's Uncertainty Principle). The second term is due to the tangential velocity of the gas atom at effective temperature T due to its thermal energy. This effective temperature is usually much higher than that of the entire imaging gas, which is at near room temperature. The kinetic energy of the gas atoms approaching the tip increases due to their dipole attraction toward the tip surface, and their subsequent diffuse rebounds are responsible for an effective rise of the temperature of the gas in the vicinity of the FIM tip. The collant bath shown in Figure BA is for the purpose of reducing this effective temperature of the imaging gas at the instant of ionization. Since the imaging gas atoms make several rebounds on the average before ionizing, their temperature approaches that of the tip rapidly.

Therefore, cooling the tip can improve the resolution of the FIM.

From Equation B.2, we can list the following in the order of their efficiency in reducing the resolution δ :

- 1. Working with tips of small radius r_{+} .
- 2. Using an imaging gas of smallest atomic radius (to reduce δ_0).
- 3. Using an imaging gas of very high ionization potential (large V_O).
- 4. Reducing the temperature of the tip.
- 5. Using an imaging gas of a large mass M.

 Because helium has the smallest atomic radius and the largest ionization potential of all gases (#2 and #3), it is usually picked as the imaging gas, despite its small atomic mass (#5).

D. Focusing

Projection of the field ionized gas atoms along the radially outward electric field lines in a FIM automatically insures that the FIM is basically focused at all times. Therefore, any attempt to improve the resolution when the microscope is operating can be thought of as "fine focusing." From Equation B.2 we see that $\delta_{\rm O}$ and the Heizenberg uncertainty terms are fixed by the imaging gas and the tip radius. Therefore, the only "focusing" applicable may be done by controlling the tip temperature.

Contrary to what may seem from Equation B.2, the lowest possible tip temperature does not always lead to the smallest resolution. In the qualitative argument given below we explore why for a given tip material and imaging gas there exists an optimum range of tip temperatures for best resolution.

Figure BC shows [after Müller (72)] the surface of the FIM tip as the very high electric field at the surface has partially drawn back the conduction electrons into the metal, exposing the positive ion cores of the surface atoms. The ionization probability for the gas atoms over the surface is indicated by the density of the contour lines. For example, the ionization is maximum directly over the atoms at the edge of net planes and increases towards the critical distance $\mathbf{x}_{\mathbf{C}}$. Below $\mathbf{x}_{\mathbf{C}}$ no contour lines are shown since this is the forbidden ionization zone. As shown in Figure BC, the impression of the surface structure on the ionization probability density is also maximum at $\mathbf{x}_{\mathbf{C}}$, i.e., gas atoms ionizing high above $\mathbf{x}_{\mathbf{C}}$ do not contribute much to the resolution of the microscope.

As the incoming gas atom A approaches the metal, its normal velocity component given by $F(\alpha/M)^{\frac{1}{2}}$ (F = electric field, M = mass of A, α = polarizability of A), increases rapidly. We consider the following three cases:

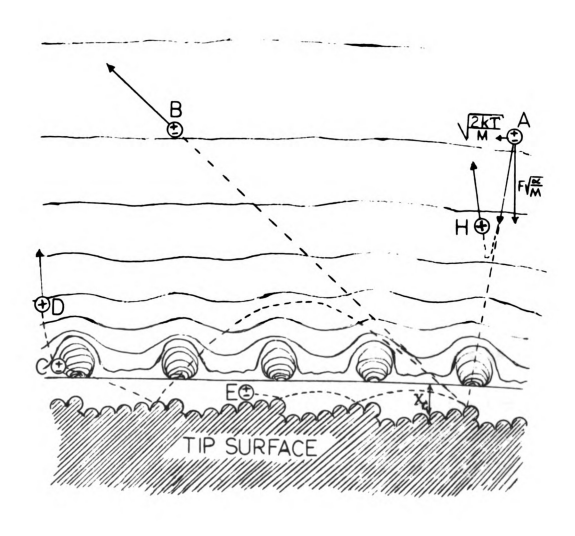


Figure BC.--(After Muller); Motion of the imaging gas atoms near the tip surface.

1. Tip temperature is too high (e.g., 100K or higher).

The atom will diffusely rebound without losing enough of its kinetic energy (shown as B). If it ionizes, it will have a large tangential velocity with the resulting loss of resolution.

2. Tip temperature is sufficiently low (5 to 20K for He on tungsten).

The incoming atom loses enough of its kinetic energy on the frst rebound that it will be pulled back to the surface by dipole attraction for more rebounds losing more energy. If it ionizes, it will be close to the surface (shown as C) and the ion (shown as D) will travel near normal to the surface.

3. Tip temperature is too low (e.g., 4.2K for neon as imaging gas).

The incoming atom may "condense" on the tip surface (shown as E) and will not be able to ionize (below $\mathbf{x}_{\mathbf{C}}$). Moreover, the FIM image is then mostly formed by atoms like H ionizing upon their first approach and partly at large distances from the tip. Degradation of the resolution results from either or both of these effects.

E. Field Evaporation

Next to the process of field ionization, field evaporation is the most important physical effect in field ion microscopy. It is a process in which an atom

on the surface of the FIM tip tunnels out of the metal leaving one or more of its electrons behind.

The two factors which most strongly affect the rate of field evaporation are the electric field at the surface and the tip temperature. In this case the electric field shapes the potential barrier through which the atom has to tunnel, and the tip temperature determines the frequency with which the atom strikes the barrier.

Following is a brief review of some of the most important aspects of field evaporation:

- 1. Resolution of a FIM is critically dependent on imaging by radial projection which requires a hemispherical, atomically smooth specimen. Conventionally prepared samples are far from such perfection, but they can be field evaporated to nearly perfect end forms. Microprotrusions and nonuniformities on the surface create extremely high local electric fields causing the atoms forming these nonuniformities to field evaporate.
- 2. The surface of the specimen would normally be covered with impurity atoms left from handling and preparation. Field desorption (term used when the evaporated atom is an impurity) clears the surface of such impurities.
- 3. The evaporation field is nearly constant for a given tip material, with variations coming from

impurities. Since the field necessary for obtaining a FIM image is determined by what imaging gas is used, it is clear that for observing a stable image of a specimen, its evaporation field must exceed the ionization field of the imaging gas. For example, with He (ionization field = 4.4v/Å) as the imaging gas, no stable image of gold (evaporation field = 3.5v/Å) can be obtained.

Field induced chemical reactions have so far plagued efforts to observe easily evaporating materials by using non-inert, low ionization field gases as the imaging gas. The effect of field induced reactions on the FIM image can be observed in a FIM using an inert imaging gas if the microscope has not been properly evacuated prior to the introduction of the imaging gas. The contaminant gases remaining in the microscope chemically etch the surface of the tip at a greatly enhanced rate due to the electric field, resulting in very unstable images (73). For this reason conventional FIMs are equipped with a sophisticated pumping system and are bakeable so that they can be pumped down to ultrahigh vacuum (p < 10^{-8} torr) before the very pure imaging gas (p $\approx 10^{-3}$ torr) is introduced.

